SARM1 activation and its downstream pathways are distinct in neuronal compartments

Authors:

Takashi Miyamoto[1], Chaeyoung Kim[1], Johann Chow[1], Jason C Dugas[1], Jack DeGroot[1], Alex L Bagdasarian[1], Arun P Thottumkara[1], Martin Larhammar[1], Meredith EK Calvert[1], Brian M Fox[1], Joseph W Lewcock[1]*, Lesley A Kane[1]*

[1]Denali Therapeutics Inc., 161 Oyster Point Blvd., South San Francisco, CA, 94080, USA

*For correspondence: lewcock@dnli.com and kane@dnli.com

Abstract:

Sterile alpha and TIR motif containing 1 (SARM1) is a critical regulator of axon degeneration that acts through hydrolysis of NAD^+ following injury. Recent work has defined the structure and catalytic activity of SARM1, yet the specific pathways controlled by SARM1 following diverse neuronal insults are not well defined. Here we show that the mechanisms of SARM1 activation and downstream signaling pathways are both context and localization dependent. Endogenous SARM1 is present in axons, dendrites and cell bodies and is primarily localized to the outer mitochondrial membrane. In cultured hippocampal neurons, knockout of SARM1 protects axons from degeneration by treatment with mitochondrial toxins but does not affect the degeneration of other cell compartments. In contrast, direct activation of SARM1 leads to degeneration of axons, dendrites, and cell bodies, indicating that SARM1 is present and can be activated in these neuronal compartments. Inhibition of dual leucine zipper kinase (DLK, MAP3K12) and caspases were not protective in these paradigms, though both SARM1-dependent and independent dendrite degeneration required calpain activity. Together, these results demonstrate that SARM1 activation is not specific to axons though distinct pathways regulate degeneration in axons and dendrites.

Introduction

Distal axon degeneration following injury follows a typical pattern that was originally termed Wallerian degeneration (Coleman and Höke, 2020). For many years following its discovery, it was believed that this degeneration was a passive process, but this rapidly changed after the identification of a mutant mouse strain that had significantly delayed axon degeneration following injury, named Wallerian degeneration slow (WLDS) (Lunn et al., 1989). The WLDS mutation was subsequently shown to result in a fusion protein of ubiquitination factor E4B (Ube4b) and nicotinamide mononucleotide adenylyltransferase 1 (NMNAT1) (Mack et al., 2001). This fusion protein persists in damaged axons and has been shown to be protective in injury models of both cultured dorsal root ganglion (DRG) or superior cervical ganglion (SCG) neurons and mouse sciatic nerves (Araki et al., 2004; Babetto et al., 2010; Conforti et al., 2009). NMNAT1, an enzyme that converts nicotinamide mononucleotide (NMN) into NAD^+, is usually localized to the nucleus, but the fusion protein is diffusely localized and stabilized, resulting in active enzyme that persists in damaged axons and preserves NAD^+ levels following injury (Sasaki et al., 2009). The identification of WLDS and its enzymatic activity was the first clue that axon degeneration and NAD^+ levels are tightly associated. Further studies in SCG neurons revealed that the endogenous protein responsible for maintaining NAD^+ levels in axons is another NMNAT isoform, NMNAT2, which is degraded upon axon injury (Gilley and Coleman, 2010).

A forward genetic screen in *Drosophila melanogaster* identified the first loss-of-function mutations that slowed axon degeneration (Osterloh et al., 2012). This study identified Sterile alpha and Armadillo motif (dSarm) and its mouse ortholog Sterile alpha and TIR motif-containing protein 1 (SARM1) as a novel regulator of axon degeneration and showed that deleting dSarm/SARM1 in flies, primary mouse cortical, SCG, and DRG neurons, and mouse sciatic nerve significantly delayed axon degeneration following injury. The mechanism by which SARM1 regulates axon degeneration became more clear upon the discovery of a non-canonical NAD^+ hydrolase function of the TIR domain of SARM1 (Essuman et al., 2017). Subsequent work demonstrated that isolated

recombinant or cellular active SARM1 is capable of hydrolyzing NAD^+ into nicotinamide, adenosine diphosphate ribose (ADPR), and cyclic-ADPR (cADPR) (Essuman et al., 2018; Horsefield et al., 2019; Loring et al., 2020; Sporny et al., 2020). This role of SARM1 in NAD^+ metabolism, along with previous results from WLDS and NMNAT2, solidified SARM1 activation as a critical step in the axon degeneration pathway following injury.

Further studies in cultured SCG neurons or *in vivo* sciatic nerve have shed more light on how NAD^+ metabolism regulated axon degeneration. Following axonal injury, the degradation of NMNAT2 results in decreased NAD^+ levels and a rise in NMN (Di Stefano et al., 2015). Increased NMN subsequently results in direct activation of SARM1 (Bratkowski et al., 2020; Figley et al., 2021; Jiang et al., 2020; Loreto et al., 2021, 2020; Sporny et al., 2020; Zhao et al., 2019). Structural investigations have confirmed an allosteric binding pocket present in SARM1, which is occupied by NAD^+ under normal conditions. Replacement of NAD^+ by NMN in the allosteric pocket induces SARM1's hydrolase activity (Bratkowski et al., 2020; Figley et al., 2021; Jiang et al., 2020; Sporny et al., 2020). Based on currently available data, it is hypothesized that other pro-degenerative stimuli may also alter the NAD^+/NMN ratio to favor activation of SARM1 by NMN binding (Di Stefano et al., 2015; Figley et al., 2021).

Though much focus has been placed on the role of SARM1 in response to axon degrative stimuli such as axotomy or chemotherapy (Coleman and Höke, 2020; Krauss et al., 2020), several groups have demonstrated that mitochondrial dysfunction is sufficient to cause a robust, SARM1-dependent axon degeneration in DRG or SCG cultures (Loreto et al., 2020; Summers et al., 2014; Yang et al., 2015). These observations are consistent with data detecting SARM1 in mitochondria (Kim et al., 2007; Panneerselvam et al., 2012). However, the mechanisms that underlie the SARM1 dependent response to mitochondrial dysfunction and the impact of these pathways in other cellular compartments remain poorly defined. In the current study, we aimed to better understand the role of SARM1 in degeneration of both the axonal and dendritic compartments following mitochondrial dysfunction in CNS neurons. We show that

distinct pathways regulate degeneration in axons and dendrites following treatment with mitochondrial toxins, yet direct SARM1 activation is sufficient to induce degeneration in both cellular compartments.

Results

SARM1 is present in all neuronal compartments and is an outer mitochondrial membrane-associated protein

Our understanding of SARM1 function comes predominantly from studies in DRG/SCG neurons as a model system (Coleman and Höke, 2020; Gerdts et al., 2016; Krauss et al., 2020), which are a population of sensory neurons with a single axon that bifurcates into two branches. To better define the expression and function of SARM1 in CNS neurons, we began by examining the subcellular localization of SARM1 in cultured primary hippocampal neurons (hereafter referred to as “neurons”). These neurons have a complex morphology with processes that can be definitively identified as axons or dendrites through use of appropriate markers. First, we examined the expression of endogenous SARM1 in wildtype (WT) neurons and observed weak, but seemingly specific signal throughout the cells (Figure 1 - figure supplement 1). Next, we moved to a 1:1 ratio mixed culture of wildtype (WT) and SARM1 knockout (KO) neurons which allowed us to both confirm the specificity of the SARM1 antibody by observing cells with (Figure 1A, arrow) and without (Figure 1A arrowhead) signal and to better observe morphological details of each neuron. Using super-resolution microscopy, we then investigated the presence of SARM1 in neuronal compartments marked by axonal (SMI312) and dendrite (MAP2) markers and found that endogenous SARM1 is present in both axons, dendrites, and cell bodies (Figure 1A).

SARM1 contains an N-terminal mitochondrial targeting sequence (Panneerselvam et al., 2012) and co-localizes with mitochondria in a variety of cell types (Kim et al., 2007; Panneerselvam et al., 2012). To confirm that SARM1 is indeed associated with mitochondria, we utilized biochemical methods to isolate crude mitochondria from either Neuro-2a (N2a) cells or neurons. In both cases, we observed

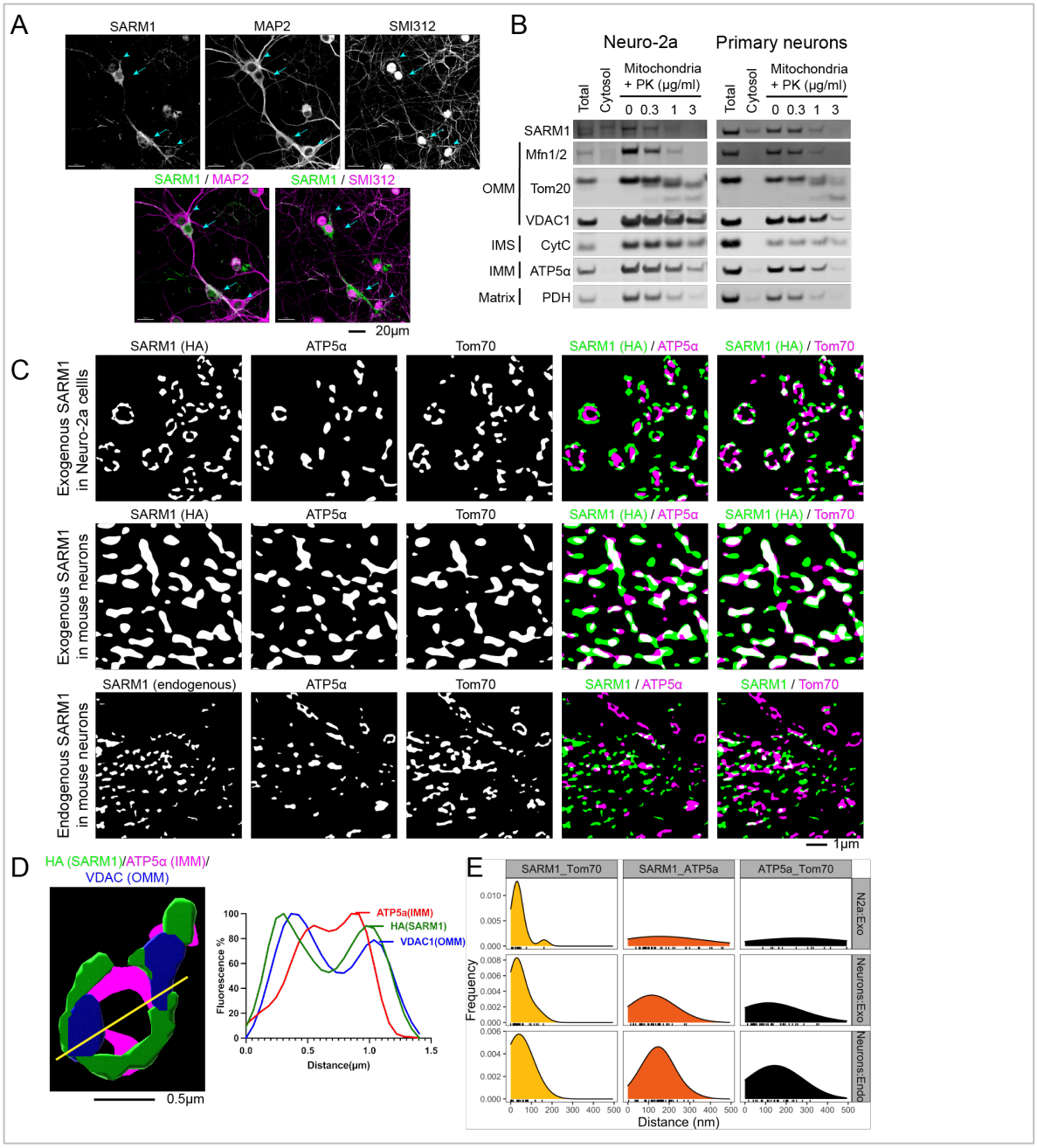

Figure 1. SARM1 is located at the outer mitochondrial membrane. (**A**) Representative images of the mixed culture of wildtype and SARM1 KO primary mouse hippocampal neurons that were immunostained for endogenous SARM1, axonal (SMI312), and dendritic (MAP2) marker proteins. Arrows and arrowheads point at wildtype and SARM1 KO neurons, respectively. (**B**) Representative western blot images of crude mitochondrial fraction prepared from Neuro-2a (N2a) and neurons that was treated with various concentrations of proteinase K (PK). Total lysate (Total) and cytosolic fraction (Cytosol) were also included. SARM1's sensitivity to PK-mediated degradation was assessed along with mitochondrial proteins of known sub-mitochondrial localization. (**C**) Representative super-resolution microscopy images of N2a and neurons that were immunostained for exogenous (anti-HA) or endogenous SARM1, outer mitochondrial marker Tom70, and inner mitochondrial marker ATP5α. (**D**) A representative super-resolution microscopy image of immunostained mitochondrion (left) and an example graph showing the immunostaining intensity of the yellow line shown in the image (right). The distance between two proteins

were defined by the distance between the two closest maxima. (**E**) Density plots showing the distribution of distances between the pairs of proteins indicated on top in three different cultured cell systems indicated on the right. N2a:Exo and Neuron:Exo indicate that exogenous HA-tagged SARM1 was used to measure the distance between endogenous Tom70 and ATP5α in N2a cells and wildtype neurons, respectively. Neurons:Endo indicates that endogenous SARM1 was used to measure the distance between endogenous Tom70 and ATP5α in the mixed culture of wildtype and SARM1 KO neurons. Data are from n=1 biological replicate in each cultured cell system.

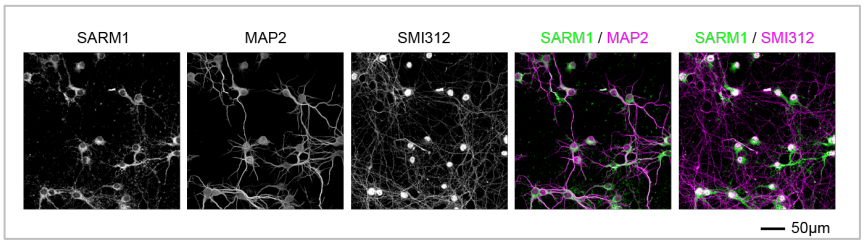

Figure 1 – Figure supplement 1. Representative images of the wildtype neuron culture that were immunostained for endogenous SARM1, axonal (SMI312), and dendritic (MAP2) marker proteins.

Figure 1—source data 1. Raw data related to Figure 1E.

Figure 1—source data 2. Original image files of the Western blots shown in Figure 1B and a PDF file showing full blots with cropped areas indicated.

an enrichment of endogenous SARM1 protein in the mitochondrial fraction (Figure 1B). When intact mitochondria were subjected to ProteinaseK (PK) digestion SARM1 displayed a sensitivity similar to the outer mitochondrial membrane (OMM) protein mitofusin (Mfn)1/2 (Figure 1B). This is consistent with previously reported localization of virally expressed SARM1 construct (Gerdts et al., 2013). However, proteins known to localize to inner mitochondrial compartments were also partially digested by PK (Figure 1B), which prevented definitive conclusions on the localization of SARM1 by this method. We thus used super resolution microscopy to assess the submitochondrial localization of endogenous SARM1 in neurons and exogenous HA-tagged SARM1 (SARM1-HA) expressed in N2a and neurons (Figure 1C-E). In all three instances, SARM1 was found closest to the OMM marker Tom70 and was further from the inner-membrane space (IMS)-localized ATP5α (Figure 1D-E). Therefore, we concluded that SARM1 is primarily localized to the OMM in both N2a cells and hippocampal neurons.

SARM1 activation by mitochondrial dysfunction results in differential neuron sensitivity

Previous studies have shown that SARM1 can be activated via disruption of mitochondrial function (Loreto et al., 2020; Sasaki et al., 2020; Summers et al., 2014). To gain a better understanding of the consequences of SARM1 activation induced by mitochondrial dysfunction in hippocampal neurons, we exposed cells to two different mitochondrial toxins and assessed the extent of degeneration by immunostaining for markers of axons (SMI312) and dendrites (MAP2), as well as quantifying nuclear condensation (DAPI). Specifically, neurons were exposed to increasing concentrations of rotenone (Complex I inhibitor) or a combination of antimycin/oligomycin (AO, Complex III and V inhibitors) for 16 hours. This technique allowed us to observe the sensitivity of each neuronal compartment to these degenerative mitochondrial insults. Both toxin treatments caused the degeneration of axons and dendrites with complete degeneration occurring at similar concentrations in both cellular compartment (50 nM for rotenone and 10 nM for AO). Nuclear condensation, indicative of cell death, also occurred following compound treatment and coincided with axon/dendrite degeneration (Figure 2A-B). SARM1 KO neurons displayed robust protection from axon degeneration compared to WT following treatment with both rotenone and AO but showed no difference in the degeneration of dendrites or condensation of nuclei (Figure 2A-B). Lentiviral expression of full-length human WT SARM1 but not the catalytically dead SARM1^{E642A} mutant (Essuman et al., 2017) in SARM1 KO neurons was capable of restoring axon degeneration, demonstrating that axonal degeneration is a result of SARM1's NAD^+ hydrolase activity (Figure 2C). Consistent with this, a recently reported SARM1 inhibitor 3-iodo-1H-pyrrolo[2,3-c]pyridine that prevents NAD^+ hydrolysis (Hughes et al., 2019) also prevented axon degeneration in rotenone treated WT neurons in a dose-dependent manner (Figure 2D). Together, these data demonstrate that the catalytic activity of SARM1 drives degeneration of axons but not dendrites following mitochondrial dysfunction.

To better understand the mechanisms underlying the differential sensitivity of axons and dendrites/cell bodies in SARM1 KO, we first examined the impact of SARM1 depletion

on mitochondrial membrane potential (ΔΨ). No difference in ΔΨ in the rotenone treatment for either genotype was observed, as ΔΨ was lost to a similar degree in both WT and SARM1 KO following AO treatment (Figure 2E). Cellular NAD(H) levels (NAD^+ and NADH) were also depleted in both WT and SARM1 KO neurons treated with rotenone (Figure 2F), indicating that the majority of NAD(H) loss caused by

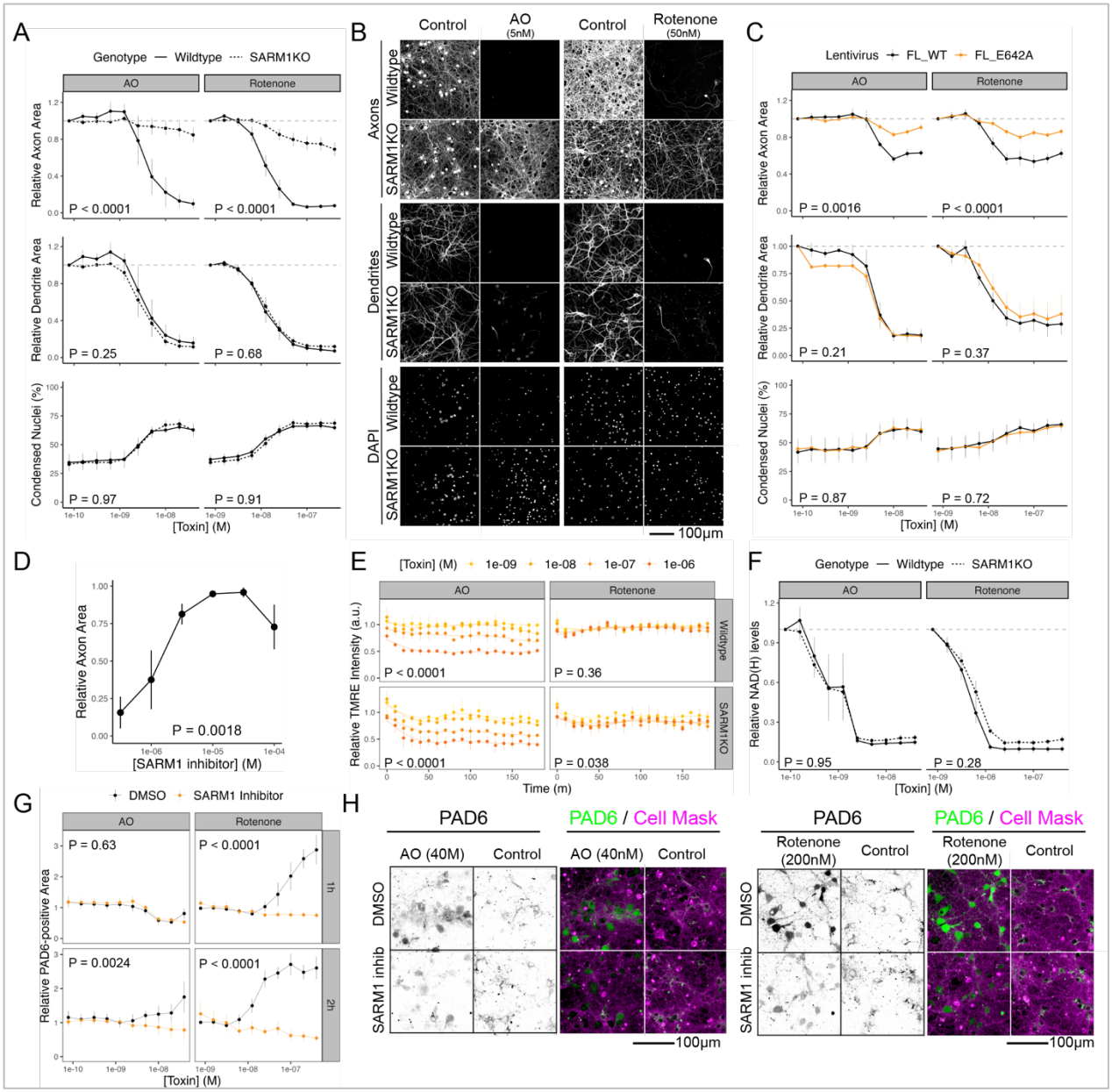

Figure 2. Mitochondrial toxins induce SARM1-dependent and -independent degeneration pathways in neuronal compartments. (**A-C**) Relative levels of immunostained axons and dendrites, and proportion of condensed nuclei in neurons that were treated with various concentrations of the combination of antimycin A and oligomycin (referred to as "AO") or rotenone for 16 hours. (**A**) Wildtype and SARM1 KO neurons were compared. (**B**) Representative images. (**C**) SARM1 KO neurons infected with lentivirus encoding full-length wildtype (FL_WT) or hydrolase-deficient E642A (FL_E642A) SARM1. (**D**) Relative

immunostained axon areas in wildtype neurons treated with 100nM rotenone and various concentrations of the SARM1 inhibitor for 16 hours. (**E**) Relative TMRE intensity changes and (**F**) cellular NAD(H) levels of wildtype or SARM1 KO neurons, that were treated with various concentrations of AO or rotenone. (**G**) Relative levels and (**H**) representative images of PAD6, a fluorescent product generated by PC6 and SARM1's NAD^+ hydrolase activity, in wildtype neurons treated with various concentrations of mitochondrial toxins for 1 or 2 hours. Some neurons were also pretreated with SARM1 inhibitor for 5min. Statistical significance of differences among groups were determined by two-way ANOVA using (**A, F**) genotype and toxin doses, (**C**) lentivirus and toxin doses, (**E**) toxin doses and duration, or (**G**) SARM1 inhibitor treatment and toxin doses, as two independent variables. P values shown in panels are for the effects of the former independent variables. In (**D**), statistical significance of SARM1 inhibitor's effect was determined by one-way ANOVA using the dose of SARM1 inhibitor as an independent variable. Numbers of biologically independent experiments (n) are (**A**) 5 (AO), 10 (Rotenone) (**C**) 5 (AO), 6 (Rotenone), (**D**) 4, (**E**) 3(WT) and 2 (KO), (**F**) 4 (AO), 6 (Rotenone), (**G**) 4 (AO), 5 (Rotenone). Data are mean ± SEM.

Figure 2—source data 1. Raw data related to Figure 2.

mitochondrial toxins is not SARM1-dependent. This was surprising, as axon degeneration is dependent on the NAD^+ hydrolase activity of SARM1 (Figure 2C) and suggests that SARM1 KO preserves only a small pool of axonal NAD(H) that we are not able to observe in whole cell analysis.

Immunostaining indicated that SARM1 protein is present in both axons and dendrites (Figure 1A), indicating that subcellular localization does not explain the observed differential sensitivity. Therefore, we next sought to directly measure the levels of SARM1 activity in each neuronal compartment following mitochondrial dysfunction using the recently identified PC6/PAD6 probe (Li et al., 2021). PAD6 is formed as an adduct of PC6 and ADPR generated by SARM1 upon NAD^+ hydrolysis, resulting in a red shift in fluorescence, which allows direct measurement of SARM1 activity in live cells (Li et al., 2021). Both mitochondrial toxins (AO and rotenone) increased the PAD6 fluorescence after 2 hrs, with rotenone eliciting a more robust signal that was visible 1hr after compound treatment (Figure 2G, H). PAD6 signal was observed in both cell bodies and neurites (Figure 2H) suggesting that SARM1 activation is not differentially regulated in different neuronal compartments following mitochondrial dysfunction and that the observed axon-only protection of the SARM1 KO is not due to activation only occurring in axons. Addition of a SARM1 inhibitor prevented the increase in PAD6 fluorescence, confirming the specificity of this probe.

Direct SARM1 activation results in degeneration of multiple neuron compartments

Although SARM1 KO neurons displayed differential sensitivity of cellular compartments to mitochondrial toxins, the PAD6 marker suggested that SARM1 activation occurred in all cellular compartments. To gain a better understanding of the consequences of SARM1 activation in axons, dendrites and cell bodies, we directly activated SARM1 using CZ-48 or Vacor, two cell permeable compounds that have been reported to mimic NMN, the endogenous SARM1 activator (Buonvicino et al., 2018; Loreto et al., 2021; Zhao et al., 2019). Interestingly, both compounds resulted in the SARM1-dependent degeneration of both axons and dendrites. Robust degeneration occurred in WT but not SARM1 KO neurons unless cells were treated with very high concentrations of Vacor, presumably because of an off-target toxicity (Figure 3A-B). Vacor also caused a SARM1-dependent increase in condensed nuclei, suggesting that in this setting SARM1 activation can be sufficient to drive cell death in addition to axon degeneration (Figure 3A-B). All neuronal compartments (axons, dendrites, and cell bodies) had similar sensitivity to Vacor, with some degeneration evident at ~2 μM and maximal degeneration occurring at 6.25 μM.

CZ-48 was not as potent a degeneration stimulus as Vacor (Figure 3C-D), but simultaneous addition of the nicotinamide phosphoribosyltransferase (NAMPT) inhibitor FK866 potentiated the degeneration observed following CZ-48 treatment (Figure 3E). This effect was presumably a result of lower NAD^+ levels allowing better access to the SARM1 allosteric binding site of CZ-48 (Figley et al., 2021; Jiang et al., 2020; Sporny et al., 2020). Unlike in the mitochondrial toxin paradigm, NAD(H) loss was SARM1-dependent in neurons treated with Vacor and CZ-48 (Figure 3F), indicating that in this assay total cell NAD(H) accurately represents SARM1 activity. As expected, both SARM1 agonists (CZ-48 and Vacor) caused an activation of SARM1 activity as measured by an increase in PAD6 fluorescence in both cell bodies and neurites that was largely blocked by a SARM1 inhibitor (Figure 3G-H).

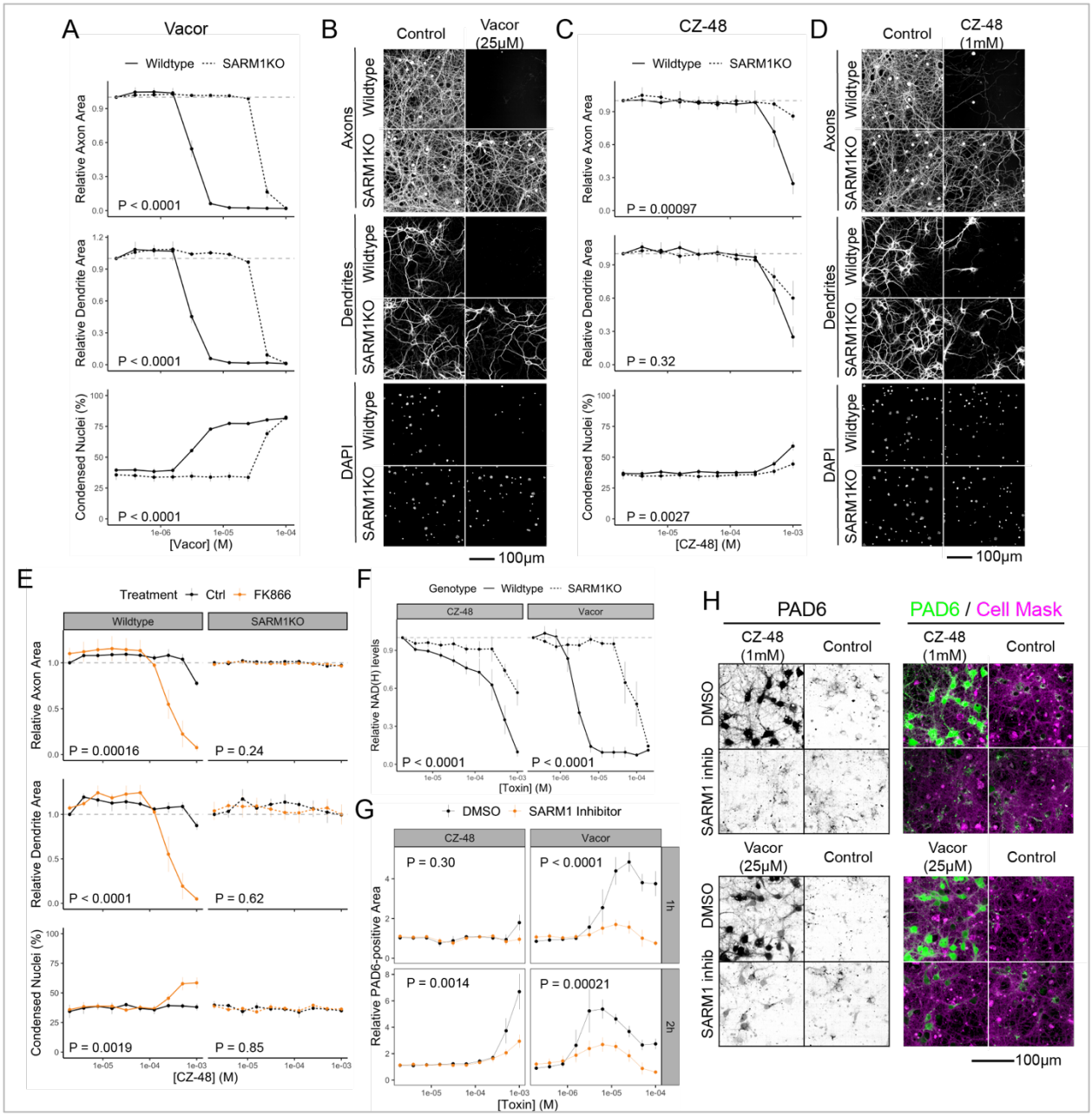

Figure 3. SARM1 activation degenerates all neuronal compartments. (**A-E**) Relative levels of immunostained axons and dendrites, and proportion of condensed nuclei in neurons that were treated with various concentrations of (**A, B**) Vacor, (**C, D**) CZ-48, or (**E**) CZ-48 in the presence of the NAMPT inhibitor FK866 (100nM). Wildtype and SARM1 KO neurons were compared after (**A-D**) 16-hour or (**E**) 8-hour treatment. Representative images are shown in (**B, D**). (**F**) Cellular NAD(H) levels of wildtype and SARM1 KO neurons that were treated with various concentrations of CZ-48 or Vacor for 16 hours. (**G**) Relative levels and (**H**) representative images of PAD6 in wildtype neurons treated with various concentrations of CZ-48 or Vacor for 1 or 2 hours. Some neurons were also co-treated with SARM1 inhibitor. Statistical significance of differences among groups were determined by two-way ANOVA using (**A, C, F**) genotype and toxin doses or (**E, G**) pharmacological treatment (**E**: FK866 and **G**: SARM1 inhibitor) and toxin doses, as two independent variables. P values shown in panels are for the effects of

the former variables. Numbers of biologically independent experiments (n) are (**A**) 4, (**C**) 5, (**E**) 3, (**F**) 3 (CZ-48), 6 (Vacor), (**G**) 4 (CZ-48), 5 (Vacor). Data are mean ± SEM.

Figure 3—source data 1. Raw data related to Figure 3.

Distinct pathways control differential sensitivity following mitochondrial dysfunction or direct SARM1 activation

SARM1 is present and activated in all compartments following mitochondrial dysfunction or activation by NMN analogs. Following mitochondrial dysfunction SARM1 knockout is only protective in axons, indicating that distinct pathways must control degeneration of each neuron compartment. To better define these mechanisms, we investigated pathways that have previously been implicated in axon degeneration: DLK/JNK, caspases and calpains.

Both DLK (Ghosh et al., 2011; Watkins et al., 2013) and caspase (Simon et al., 2012) activation have been linked to axon degeneration and neuronal apoptosis, and DLK activity promotes SARM1-mediated DRG axon degeneration following mitochondrial dysfunction (Summers et al., 2020). To test the relevance of these pathways in our hippocampal neuron setup, cells were treated with either a well-characterized DLK inhibitor (GNE-3511, Figure 4A, B – figure supplement 1A, B) or a pan-caspase inhibitor (QVD: Q-VD-OPH, Figure 4C, D – figure supplement 1C, D) in the presence of rotenone or Vacor. In this paradigm, these inhibitors had no effect on degeneration of axons, dendrites or cell bodies in either genotype, even though both compounds inhibited activation of caspases in DRG neurons after deprivation of NGF (Figure 4 – figure supplement 2). Therefore, DLK and caspases are not essential drivers of degeneration in hippocampal neurons following mitochondrial dysfunction or direct SARM1 activation.

We next examined Calcium (Ca^{2+}) influx and activity of calpains, which are Ca^{2+}-dependent proteases, based on their known contribution to neuron degeneration following injury or mitochondrial dysfunction in DRG neurons (Loreto et al., 2015; Summers et al., 2014; Vargas et al., 2015; Yang et al., 2013). Interestingly, addition of a calpain inhibitor prevented degeneration of dendrites following rotenone treatment but

had no effect on axon degeneration or nuclear condensation (Figure 5A – figure supplement 1A). This protection was not SARM1-dependent as it occurred in both WT and SARM1 KO neurons. Surprisingly, calpain inhibition elicited similar dendrite-specific protection following Vacor treatment, indicating that calpain activation in dendrites occurs downstream of SARM1 in this context (Figure 5B - figure supplement 1B).

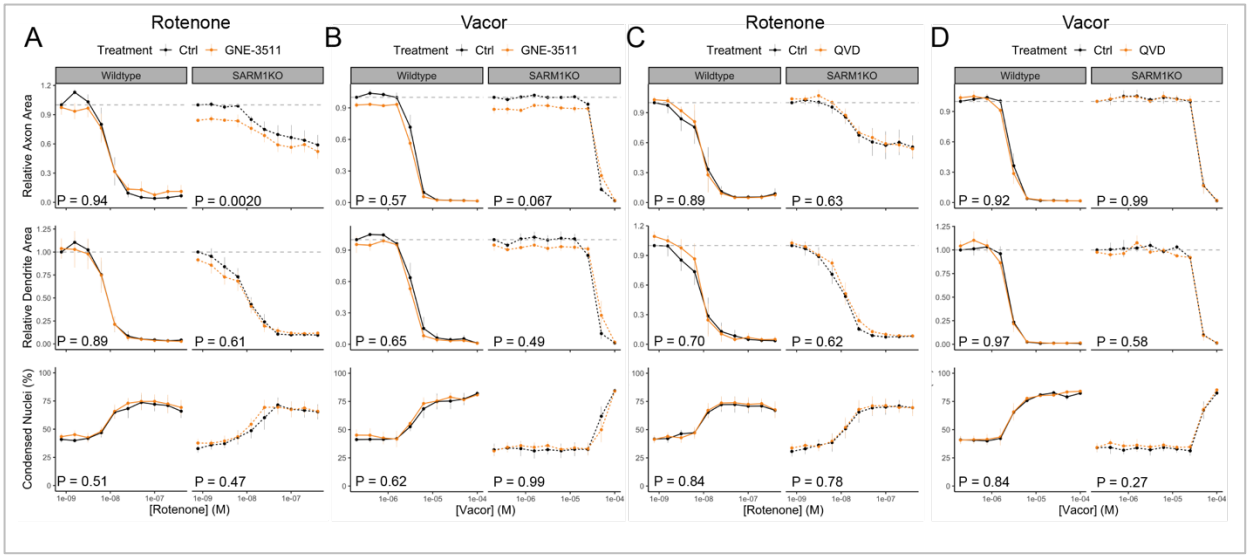

Figure 4. DLK and caspase are not required for degeneration induced by rotenone or Vacor. Relative levels of immunostained axons and dendrites, proportion of condensed nuclei, and their representative images of wildtype or SARM1 KO neurons that were treated with various concentrations of rotenone or Vacor. Neurons were also co-treated with (**A, B**) the DLK inhibitor GNE-3511 (1μM), or (**C, D**) a pan-caspase inhibitor QVD (10μM) for 16 hours. Statistical significance of differences among groups were determined by two-way ANOVA using pharmacological treatment (**A, B**: GNE-3511 and **C, D**: QVD) and toxin doses as two independent variables. P values shown in panels are for the effects of pharmacological treatments. Numbers of biologically independent experiments (n) are (**A**) 4 (Wildtype), 5 (SARM1 KO), (**B-D**) 3-4 (both Wildtype and SARM1 KO). Data are mean ± SEM.

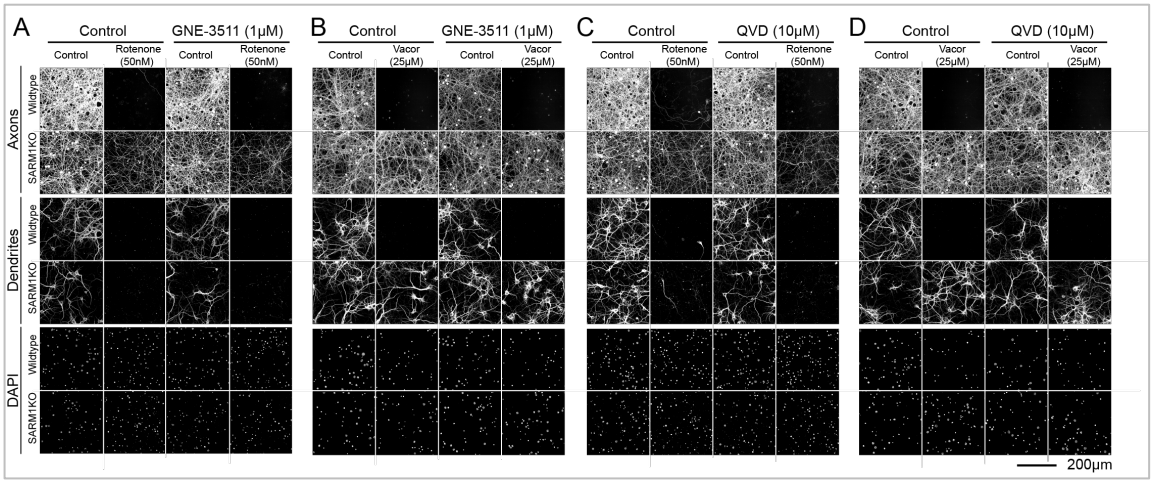

Figure 4 – Figure supplement 1. Representative images from Figure 4.

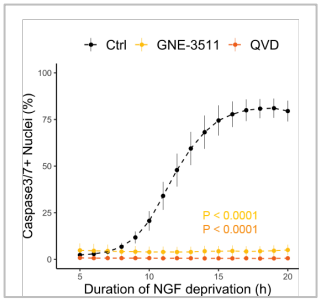

Figure 4 – Figure supplement 2. GNE-3511 (500nM) and QVD (1μM) prevented activation of caspases in primary mouse dorsal root ganglia neurons that were deprived of nerve growth factor. Statistical significance of effects by inhibitors were determined by two-way ANOVA using inhibitor treatment and duration of NGF-deprivation as two independent variables. Each inhibitor-treated group was compared to the control group by the Dunnett's post-hoc test. P values shown in panels are for the comparison between control and each inhibitor-treated group and are color-matched. Numbers of biologically independent experiments (n) are 6 (Ctrl), 5 (GNE-3511), and 3 (QVD). Data are mean ± SEM.

Figure 4—source data 1. Raw data related to Figure 4 and Figure 4 – Figure supplement 2.

Direct activation of SARM1 by CZ-48/FK866 also resulted in calpain-dependent dendrite degeneration (Figure 5 – figure supplement 2). To further confirm this, we measured calpain activity in the neuron lysates by the cleavage of α-fodrin, a substrate of calpain that is present in both dendrites and axons (Cryns et al., 1996) (Figure 5 - figure supplement 3). The ratio between cleaved and total α-fodrin, following rotenone treatment was not different between WT and SARM1 KO neurons, but was significantly blunted in SARM1 KO neurons following Vacor treatment (Figure 5C, D). Together, these results confirm calpain activation occurs following both rotenone and Vacor treatment. In addition, since the cleavage of α-fodrin is only protected by SARM1 KO in the context of direct activation via Vacor (both axons and dendrites are protected) and not in the rotenone paradigm (only axons are protected), this argues that the downstream calpain activation is specific to dendrites.

To confirm that calpain activation can occur downstream of SARM1, we delayed the addition of either a SARM1 or calpain inhibitor until after activation of SARM1 (Figure 5E, F, figure supplement 4). Delayed addition of a SARM1 inhibitor protected axons when applied after rotenone or Vacor treatment (up to 3h and 1.5h, respectively), but only protected dendrites in the context of Vacor activation (Figure 5E, F, yellow

shading). When added after rotenone, Calpain inhibitor III offered little protection of axons (Figure 5E) but was able to protect dendrites even when added up to 1h into rotenone treatment (Figure 5F, left orange shading). In the context of Vacor activation, there was a window beyond SARM1 inhibition where calpain inhibition retained its protective effect (Figure 5F, right orange shading), indicating that calpain activation is downstream of SARM1.

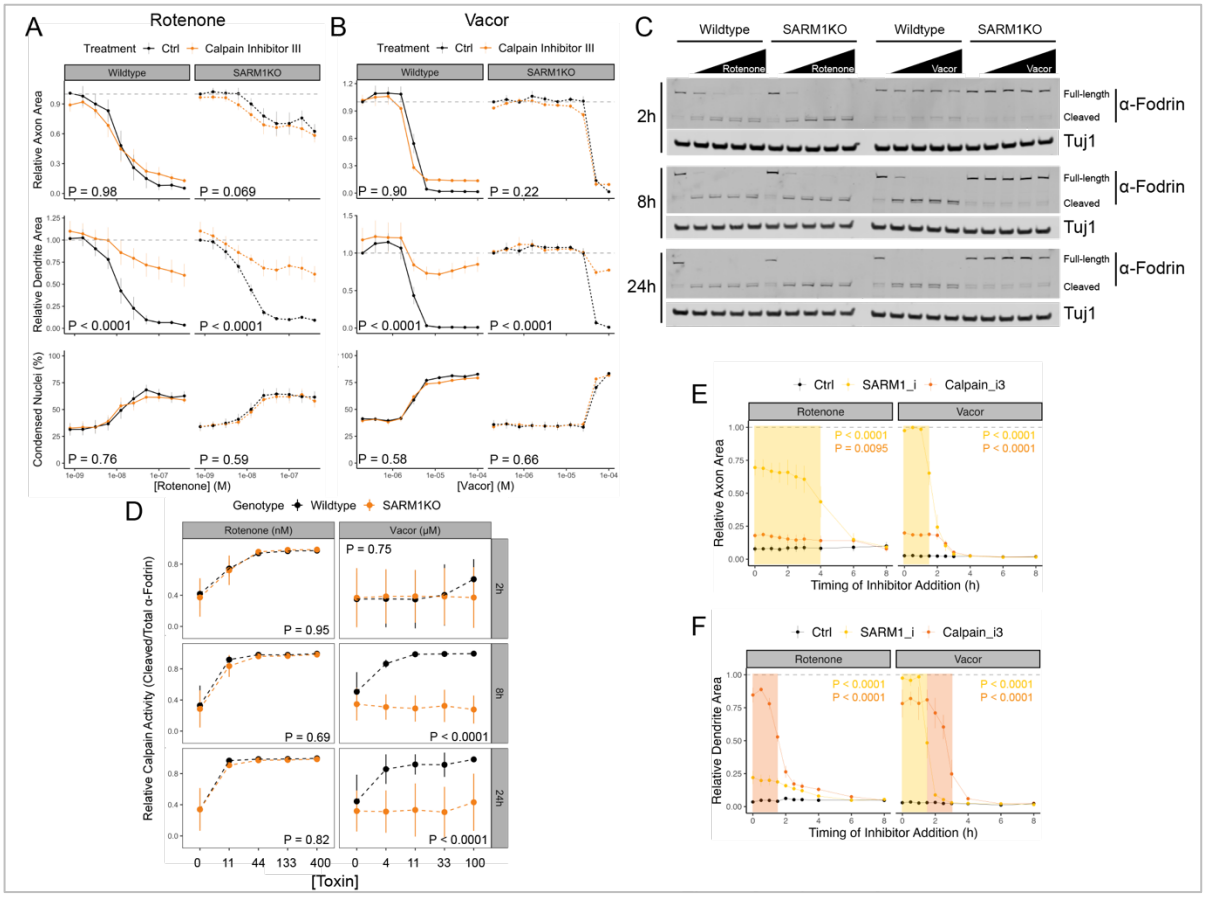

Figure 5. Calpain activity is required for dendrite degeneration downstream of SARM1 activity. (**A, B**) Relative levels of immunostained axons and dendrites, and proportion of condensed nuclei of wildtype or SARM1 KO neurons that were treated with various concentrations of (**A**) rotenone or (**B**) Vacor. Neurons were also co-treated with calpain inhibitor III (30μM) for 16 hours. (**C**) Representative western blot images of α-Fodrin in wildtype and SARM1 KO neurons treated with rotenone or Vacor. (**D**) Relative calpain activity based on the ratio of cleaved and total (sum of full-length and cleaved) α-Fodrin. (**E, F**) Relative levels of immunostained (**E**) axons and (**F**) dendrites in wildtype neurons that were treated with rotenone (100nM) or Vacor (30μM) for 8 hours. Some neurons were also treated with calpain inhibitor III (Calpain_i3, 30μM), SARM1 inhibitor (SARM1_i, 10μM) or vehicle (Ctrl) at various time points after toxin treatment. The durations for axons or dendrites to be protected from degeneration by delayed inhibitor addition are shaded in color-matched boxes. Statistical significance of differences among groups were determined by two-way ANOVA using (**A, B, E, F**) pharmacological treatment and toxin doses, or (**D**) genotype and toxin doses as two independent variables. P values shown in panels are for the effects of pharmacological treatments. In (**E, F**), Each inhibitor-treated group was compared to the control group

(Ctrl) by the Dunnett's post-hoc test. P values shown in panels are for the comparison between control and each inhibitor-treated group and are color-matched. In (**F**), the duration of delayed inhibitor addition was longer for Calpain inhibitor III (2.5h, P < 0.0001 at T= 0 - 2.5h and P = 0.43 at T=3h) than it was for a SARM1 inhibitor (1.5h, P < 0.0001 at T=0 - 1.5h and P=1.0 at T=2h), determined by the Tukey's post-hoc test applied between the two inhibitor-treated groups. Numbers of biologically independent experiments (n) are (**A**) 7 (Wildtype), 6 (SARM1 KO), (**B**) 4 (both Wildtype and SARM1 KO), (**D**) 3-4 (both wildtype and SARM1 KO at all three time points), and (**E, F**) 3. Data are mean ± SEM.

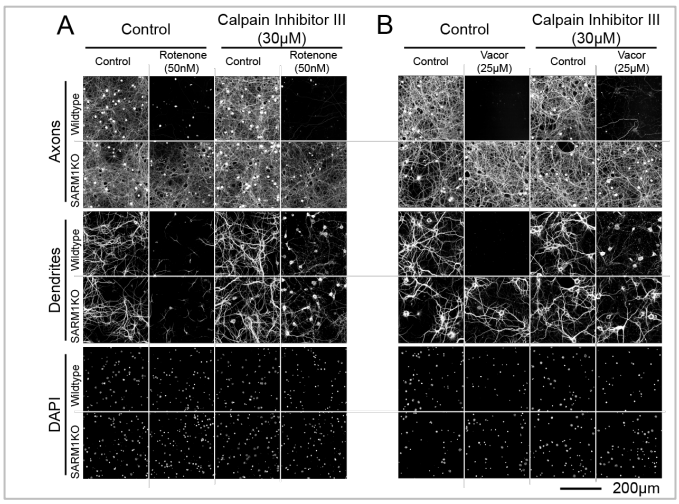

Figure 5 – Figure supplement 1. Representative images for Figure 5 (**A, B**).

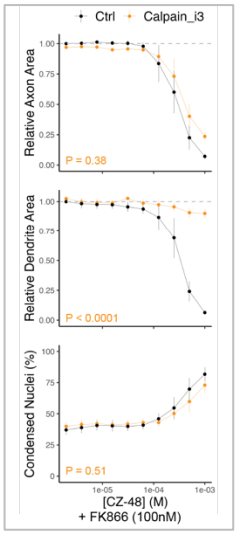

Figure 5 – Figure supplement 2. Relative levels of immunostained axons and dendrites, and proportion of condensed nuclei in wildtype neurons that were treated with various concentrations of CZ-48 in the presence of FK866 (100nM) for 8 hours. Statistical significance of differences among groups were determined by two-way ANOVA using pharmacological treatment (Ctrl vs. Calpain_i3) and toxin doses as two independent variables. P values shown in panels are for the effects of Calpain Inhibitor III (Calpain_i3). Numbers of biologically independent experiments (n) are 5. Data are mean ± SEM.

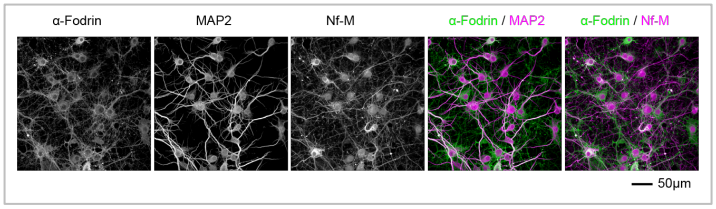

Figure 5 – Figure supplement 3. Representative images of the wildtype neuron culture that were immunostained for α-Fodrin, axonal (SMI312), and dendritic (MAP2) marker proteins.

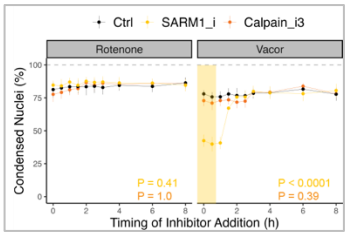

Figure 5 – Figure supplement 4. Relative levels of condensed nuclei measured along with axons (**F**) and dendrites (**G**). Statistical significance of differences among groups were determined by two-way ANOVA using pharmacological treatment and toxin doses. Each inhibitor-treated group was compared to the control group (Ctrl) by the Dunnett's post-hoc test. P values shown in panels are for the comparison between control and each inhibitor-treated group and are color-matched. Numbers of biologically independent experiments (n) are 3. Data are mean ± SEM.

Figure 5—source data 1. Raw data related to Figure 5 and Figure 5 – Figure supplements 2 and 4.

Figure 5—source data 2. Original image files of the Western blots shown and quantified in Figure 5C-D and a PDF file showing full blots with cropped areas indicated.

Calcium is required upstream of SARM1 activation, independent of Calpain activation

Multiple waves of Ca^{2+} influx have been described in axon lesion studies, a first transient wave that occurs rapidly after injury and a second prolonged one that occurs hours after injury and right before axon fragmentation (Loreto et al., 2015; Vargas et al., 2015). To examine how increases in intracellular Ca^{2+} relate to calpain activation, WT and SARM1 KO neurons were treated with EGTA in addition to either rotenone or Vacor. Unlike what was observed with calpain inhibition, EGTA treatment prevented degeneration of dendrites and cell bodies in both genotypes, but caused axon degeneration itself, making it difficult to assess its potential axon-protective effect (Figure 6A, B - figure supplement 1). These results suggested that Ca^{2+} contributed to additional aspects of pro-degeneration signaling in addition to calpain activation. To better determine the mechanisms by which Ca^{2+} influx contributes to degeneration in

this setup, we treated neurons with degeneration stimuli and either calpain inhibitors or EGTA in the presence of the PC6/PAD6 probe to determine whether Ca^{2+} contributed to SARM1 activation. As expected, direct activation of SARM1 by CZ-48 was not robustly altered by either Calpain inhibitor III or EGTA (Figure 6C, D). Calpain inhibitor III had subtle effects on the increase of PAD6 fluorescence in neurons treated with rotenone but had no effect on Vacor-induced activation (Figure 6C, D). Unexpectedly, EGTA strongly inhibited the PAD6 increase in neurons treated with either rotenone or Vacor (Figure 6C, D), indicating that Ca^{2+} increase plays an important role in SARM1 activation in both paradigms.

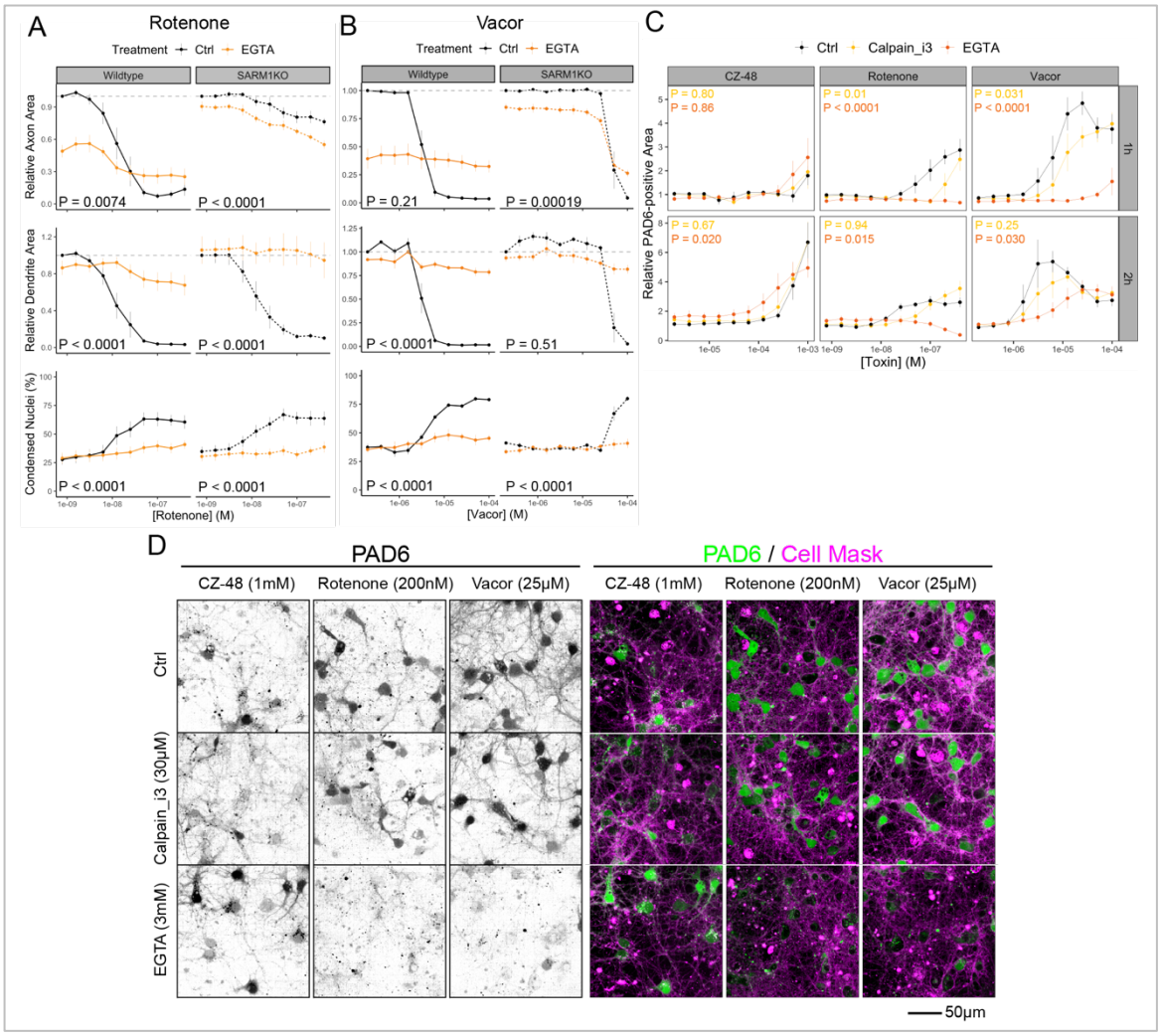

Figure 6. Calcium is required upstream of SARM1 activation. (**A, B**) Relative levels of immunostained axons and dendrites, proportion of condensed nuclei, and their representative images of wildtype or SARM1 KO neurons that were treated with various concentrations of (**A**) rotenone or (**B**) Vacor. Neurons were also co-treated with EGTA (3mM) for 8 hours. (**C**) Relative PAD6 fluorescence

levels and (**D**) representative images of PC6-loaded neurons that were treated with SARM1-activating stimuli for 1 or 2 hours. Subsets of neurons were also co-treated with inhibitors of calpain (Calpain_i3: Calpain Inhibitor III, 30μM), and calcium influx (EGTA, 3mM). Statistical significance of effects by inhibitors were determined by two-way ANOVA using inhibitor treatment and toxin doses as two independent variables. In (**A, B**), P values shown in panels are for the effects of pharmacological treatments. In (**C**), each inhibitor-treated group was compared to the control group by the Dunnett's post-hoc test. P values shown in panels are for the comparison between control and each inhibitor-treated group and are color-matched. Numbers of biologically independent experiments (n) are (**A**) 7 (Wildtype), 6 (SARM1 KO), (**B**) 3 (both Wildtype and SARM1 KO), and (**C**) 5. Data are mean ± SEM.

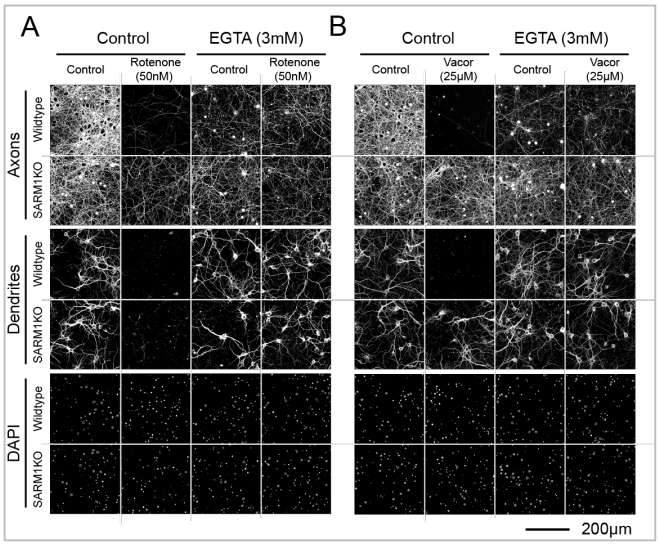

Figure 6 – Figure supplement 1. Representative images for Figure 6 (**A, B**).

Figure 6—source data 1. Raw data related to Figure 6.

Discussion

Since its identification as a critical mediator of axon degeneration, SARM1 has been studied primarily in axons (Coleman and Höke, 2020; Gerdts et al., 2016; Krauss et al., 2020). In this study we sought to understand the localization and function of SARM1 in CNS neurons with more complex cellular morphology. We demonstrate that SARM1 is expressed throughout the neuron and contributes not only to axon degeneration but also to programmed degeneration of the dendrite and the cell body in response to mitochondrial dysfunction. Calpain plays a key role in both SARM1-dependent and independent degeneration that is unique to dendrites. Lastly, we show that calcium also plays a role upstream of SARM1 activation that is distinct from calpain activation.

SARM1-dependent degeneration downstream of rotenone is consistent with the localization of SARM1 to the mitochondria (Gerdts et al., 2013; Kim et al., 2007; Panneerselvam et al., 2012), though presence of neuronal SARM1 on the OMM is surprising. SARM1 contains a mitochondrial targeting sequence (Panneerselvam et al., 2012), but no predicted transmembrane domains. Other proteins with similar properties are usually found localized to the mitochondrial matrix (Dudek et al., 2013). The pools of NAD^+ in the cytosol and matrix are independent and tightly regulated (Verdin, 2015) and the non-canonical localization of SARM1 implies that its enzymatic domains primarily access cytosolic NAD^+. This hypothesis agrees with the finding that forced dimerization of the TIR domain of SARM1 in the cytosol recapitulates axon degeneration functions (Gerdts et al., 2015; Yang et al., 2015). Understanding how SARM1 is tethered to the OMM in the absence of a transmembrane domain is complicated further by the octameric structure of the enzyme (Bratkowski et al., 2020; Figley et al., 2021; Horsefield et al., 2019; Jiang et al., 2020; Shen et al., 2021; Sporny et al., 2020). Understanding what scaffolding proteins regulate SARM1 OMM localization may prove important to understanding the overall pathway of SARM1-dependent degeneration.

SARM1 activation has been observed as a consequence of many axon degenerative stimuli including axon injury (Coleman and Höke, 2020), chemotherapy (Geisler et al., 2019; Li et al., 2021; Yang et al., 2015) and mitochondrial dysfunction (Loreto et al., 2020; Summers et al., 2014; Sur et al., 2018). Here we confirm the activation of SARM1 by mitochondrial toxins in primary CNS neurons and observe that activated SARM1 is not restricted to axons but is also present in cell bodies and neurites. Despite the ubiquitous presence of activated SARM1 following rotenone or antimycin/oligomycin treatment, it appeared to be the primary driver of degeneration only in axons. This is consistent with previous data that suggested an axon-specific role for SARM1 following mitochondrial dysfunction in DRGs, including the observation that NAD^+ and ATP are downregulated in a SARM1-dependent manner following mitochondrial dysfunction (Sasaki et al., 2020; Yang et al., 2015). Our data suggest a SARM1-independent pathway activated by mitochondrial dysfunction that dominates the degenerative

program in cell bodies and dendrites. This pathway was not affected by DLK or caspase inhibition, but required calpain activity. Mitochondria have been observed to have vastly different morphologies and dynamics in axons and dendrites which may underlie some of the divergent responses to mitochondrial dysfunction that we observed in these neuronal compartments (Seager et al., 2020).

Recently identified SARM1 agonists, CZ-48 and Vacor/VMN (Loreto et al., 2021; Zhao et al., 2019) allowed us to directly activate SARM1 in the absence of mitochondrial disruption. Treatment of neurons with these compounds resulted in SARM1-dependent degeneration of axons, dendrites, and cell bodies. This demonstrates that activation of SARM1 is sufficient to cause destruction of the entire neuron. Together with the activation of SARM1 in dendrites following rotenone treatment (Figure 2G, H) this implies that the lack of dendrite protection in SARM KO neurons is a result of additional pathways contributing to degeneration. Both SARM1-independent and SARM1-dependent dendrite degeneration were also blocked by calpain inhibition, revealing a common calpain activation as a common convergence point regulating degeneration in dendrites.

The role of calcium has been extensively studied in models of Wallerian degeneration. Models as diverse as mouse SCG/DRGs, zebrafish and flies have revealed two distinct phases of calcium influx in Wallerian degeneration (Avery et al., 2012; Loreto et al., 2015; Mishra et al., 2013; Tian et al., 2020; Vargas et al., 2015). The first phase of calcium influx is transient and proximal to the axon injury site and the second is a more widespread terminal phase of calcium influx that shortly precedes degeneration. There is clear evidence that the WLDS mutant protein (Vargas et al., 2015) or SARM1 deletion (Loreto et al., 2015) can prevent the second phase of calcium influx, but their impact on the first phase remains unclear (Avery et al., 2012; Loreto et al., 2015; Mishra et al., 2013; Tian et al., 2020; Vargas et al., 2015). Calcium influx is also required for axon degeneration caused by mitochondrial dysfunction (Summers et al., 2014). In our study, EGTA-mediated Ca^{2+} chelation was required for rotenone- or Vacor-induced SARM1 activation and strongly protected dendrites from degeneration. These observations

indicate that SARM1 activation requires a first phase of calcium influx and lead to a more sustained secondary calcium signal that results in calpain activation in dendrites. It is possible that cADPR generated by SARM1 activity (Sasaki et al., 2020) is involved in mobilizing downstream calcium fluxes as the catalytic activity of SARM1 is required for axon degeneration following rotenone.

Calcium influx has been tied to the activation of calpain proteases in Wallerian degeneration of DRG axons where calpain inhibition robustly prevents axon degeneration (Yang et al., 2013). In our primary hippocampal neuron models, we also observed a requirement for calpain activation, but surprisingly calpain inhibition did not impact axon degeneration, but was sufficient to protect dendrites. Calpain inhibition had no major effect on SARM1 activation and prevented both SARM1-independent (rotenone) and SARM1-dependent (Vacor) dendrite degeneration. Together these data indicate that calpain activation is downstream of SARM1 activation, which was substantiated by the ability of both calpain inhibitors and EGTA to block dendrite degeneration when added substantially after SARM1 activation. Why these proteases are only critical for dendrite and not axon degeneration in these paradigms is still unclear. Our data are unable to distinguish if calpains are only activated in dendrites or if the activation occurs in all compartments but is only required in dendrites. Calpains have been shown to be distributed throughout cells and have been observed to be localized in the cytoplasm, ER, Golgi or plasma membrane (Metwally et al., 2021). It is possible that there is a differential distribution of calpains that cause the differential requirement for their activity in dendrites vs axons. Further experiments to understand the relationships between calcium, calpains and SARM1 will provide insights into the mechanisms through which SARM1 can cause broad neurodegeneration vs specific axon degeneration. In this study we defined a degenerative role for SARM1 and calpains in hippocampal neurons that is both stimuli and localization dependent (Figure 7).

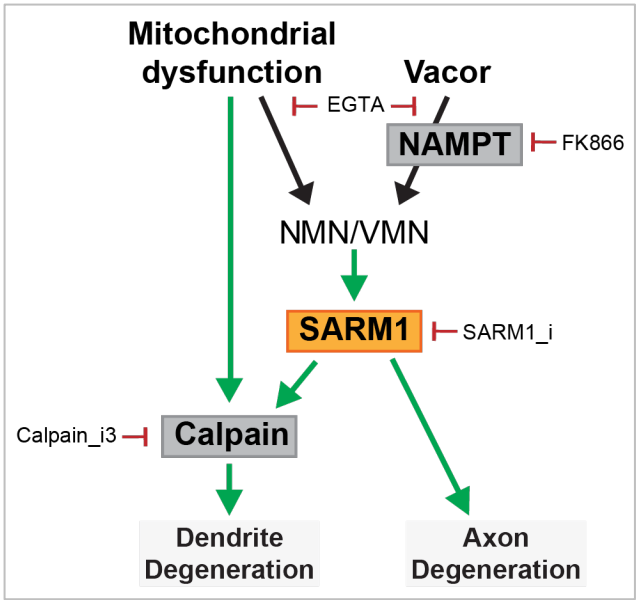

Figure 7. Distinct degeneration pathways in neuronal compartments. A diagram showing distinct degenerative pathways in different neuronal compartments, that are activated by mitochondrial toxins and direct SARM1 activation by NMN analogs in cultured mouse hippocampal neurons.

Materials and Methods

Primary hippocampal neurons

Hippocampi were dissected from E16-E18 embryos of C57BL/6, CD-1 (Charles River Laboratories), or Sarm1-deficient mice (B6. 129X1-*Sarm1*^{tm1Aidi}/J, 018069, The Jackson Laboratory) in ice-cold Hibernate E solution. Dissected hippocampi were digested with ~0.1 unit/hippocampus of papain in 1x PBS at 37°C for 10min and then incubated with DNAseI (3000 unit/ml) and HI-FBS (half the volume of papain solution) at RT for 5min. Hippocampi were dissociated by gentle pipetting (~20 strokes) in the complete NbActiv4 medium (50µl medium per hippocampus). The complete NbActiv4 medium consists of NbActiv4 (500ml) supplemented with Penicillin-Streptomycin (5ml, the final concentration at 100U/ml), Glutamax (5ml), and 5-floro-2-deoxyuridine (final concentration 1µM). Dissociated hippocampi were spun down at 500rcf at 4°C for 3min and the pellet was dissociated in the complete NbActiv4. Live cells were counted using a Cellometer Auto 2000 Cell Viability Counter (Nexcelom), and the cells were plated on PDL-coated 96-well or 384-well plates at the density of 25000 or 12500 cells/well in 100µl or 50µl of the complete NbActiv4. Hippocampal neurons were grown for 8-12 days with half-medium changes every 7 days.

Cell Lines

Neuro-2a (N2a) cells are derived from mouse (Mus musculus) neuroblasts and were purchased from ATCC (CCL-131, RRID: CVCL_0470).

Immunocytochemistry

Primary hippocampal neurons were treated with rotenone, Vacor, and/or other pharmacological tools in the complete NbActiv4 medium at 37°C and 5% CO_2 for 8-20h. After treatment, neurons were fixed with 4% paraformaldehyde (PFA) with 4% sucrose (Sigma-Aldrich, S0389) in 1x PBS at RT for 15min. Fixed neurons were washed with 1x PBS once and then blocked in the blocking buffer at RT for at least 1h. The blocking buffer consists of 5% bovine serum albumin (BSA), 0.5% Triton X100 in 1x PBS. After blocking, neurons were incubated with primary antibodies diluted in the blocking buffer

at 4°C for at least 16h. Neurons were then washed 3 times with 1x PBS, incubated with secondary antibodies diluted in the blocking buffer at RT for 1h, and then washed again 3 times with 1x PBS.

Super resolution confocal imaging and quantification of SARM1 localization

Neuro-2a or neurons were plated on PDL-coated 96-well plate (Greiner Bio-one, 655946) for super resolution confocal imaging. Immunocytochemistry was done essentially in the same way as described above, except for fixation. For super resolution confocal imaging, cells were fixed with 4% PFA with 4% sucrose in 1x PBS at RT for 10min and then 100% MeOH at 4˚C for an additional 5 min for mitochondrial staining. Immunostained cells were imaged with a laser scanning confocal microscope (Leica SP8; Leica Microsystems, Inc), acquired with a 63x/1.4 NA oil objective in LIGHTNING super-resolution mode with a pixel size of 40 nm. Images were then processed using an adaptive processing algorithm. The representative images were generated by three-dimensional reconstruction using Imaris (Bitplane). To obtain accurate mitochondrial 3D structures, we used surface rendering and fluorescence thresholding. Quantification of SARM1 localization within mitochondria was performed using ImageJ2 (National Institutes of Health), by profiling the fluorescence intensity of each channel by Plot_Multicolor4.3 (Rueden et al., 2017).

Table 1: Antibodies used

Target	Clone	Source	Identifier	RRID	Application	Concentration
α-Fodrin	3D7	Novus	NBP1-92689	AB_11031596	ICC	1:500
ATP5a	15H4C4	Abcam	ab14748	AB_301447	ICC	1:500
ATP5A1	Rb polyclonal	Proteintech	14676-1-AP	AB_2061761	ICC	1:200
Axonal neurofilaments	SMI312	BioLegend	837904	AB_2566782	ICC	1:2000
HA	F-7	Santa Cruz	sc-7392	AB_2894930	ICC	1:2000
MAP2	Chk polyclonal	Abcam	ab5392	AB_2138153	ICC	1:5000
MAP2	Rb polyclonal	Abcam	ab32454	AB_776174	ICC	1:2000
Nf-M	Rb polyclonal	BioLegend	841001	AB_2565457	ICC	1:500
SARM1	W16079A	BioLegend	696602	AB_2687069	ICC	1:100
Tom70	A-8	Santa Cruz	sc-390545	AB_2714192	ICC	1:50
VDAC1	EPR10852(B)	Abcam	ab154856	AB_2687466	ICC	1:500
Specific species	Various	Thermo Fisher Scientific	Secondary antibodies conjugated with Alexa Fluor dyes	Various	ICC	1:1000

α-Fodrin	Rb polyclonal	CST	2122S	AB_331436	WB	1:1000
ATP5a	Rb polyclonal	Proteintech	14676-1-AP	AB_2061761	WB	1:2000
Cytochrome C	7H8	Santa Cruz	sc-13560	AB_627383	WB	1:1000
Mfn1/2	3C9	Abcam	ab57602	AB_2142624	WB	1:2000
PDHA1	9H9AF5	Abcam	ab110330	AB_10858459	WB	1:2000
SARM1	W16079A	BioLegend	696602	AB_2687069	WB	1:500
Tom20	FL-145	Santa Cruz	sc-11415	B_2207533	WB	1:1000
VDAC1	EPR10852(B)	Abcam	ab154856	AB_2687466	WB	1:1000
Specific species	Various	Li-cor biosciences	Secondary antibodies conjugated with IRDyes	Various	WB	1:10000

Liquid handling (plating, feeding, fixing, and immunostaining neurons on 384-well plates)

Neurons were resuspended in the complete NbActive4 media at a density of 250000 cells/mL. A Dynamic Devices Lynx liquid handler in a sterile cabinet was used to plate cells (12500 cells /well in 50µl media) into PDL-coated 384-well clear-bottom optical plates, with gentle resuspension of cells in the source reservoir prior to transfer to promote even plating density. Cells feeding was performed in the Lynx by removing 50% of the media and gently adding the complete media slowly to avoid cell disruption every 7 days. Immunostaining was performed as described in the "Immunocytochemistry" section, using a BioTek EL406 plate washer and Agilent Bravo liquid handler, integrated by HighRes Biosolutions, to gently transfer 1x PBS or reagents to neurons at each step.

Quantification of axon/dendrite degeneration and nuclear condensation

Immunostained primary hippocampal neurons were imaged using the Opera Phenix High Content Screening System (PerkinElmer) and images were quantified using the Harmony software (PerkinElmer). To acquire fluorescent images, we used built-in acquisition protocols for DAPI (excitation/emission at 375nm/ 435-480nm), Alexa488 (488nm/ 500-550nm), Alexa568 (561nm/ 570-630nm), and Alexa647 (640nm/ 650-760nm), and water-immersion 40x objective (NA=1.1) using the confocal mode acquiring two z-slice images spaced 1µm apart. Areas of axons or dendrites were quantified by applying the built-in spot analysis on images of respective channels. Total areas of axons or dendrites were quantified per well and per plate, and normalized to

the respective control values (e.g. mean of untreated wildtype wells) per plate. All the nuclei were detected by applying the built-in nucleus detection protocol on DAPI images and further classified into condensed or normal nuclei by applying a manual linear classifier that was trained using at least 50 nuclei per group.

Quantification of PAD6 signal

Cultured neurons were incubated with PC6 (50µM) and CellMask deep red (Thermo Fisher Scientific C10046, 1:5000) for 2h prior to imaging, in the complete NbActiv4 in the humidified incubator at 37°C with 5% CO2. 1h prior to imaging, SARM1 agonist and inhibitors were added by D300e digital dispenser (Tecan) and further incubated in the incubator. PAD6 signal was imaged using the Opera Phenix Plus High Content Screening System (PerkinElmer) and images were quantified using the Harmony software (PerkinElmer). To acquire PAD6 and CellMask signal, we used built-in acquisition protocols for mTurquoise2-extended (excitation/emission at 405nm/435-550nm) and Alexa647 (640nm/ 650-760nm), respectively, and water immersion 63x (NA=1.15) under the confocal mode acquiring two z-slice images spaced 0.5µm apart, at 37°C and with 5% CO_2. PAD6-positive area was quantified first by applying an intensity threshold for mTurquoise2-extended channel to select pixels with PAD6 signal above the background, and then by measuring the total numbers of pixels per well. The PAD6-positive area was normalized to the respective control values (mean of untreated wildtype wells) per plate.

Western blot

Equal numbers of isolated mitochondria (Figure 1B) or cultured neurons (Figure 5C) underwent treatment, were lysed in equal volumes of lysis buffer (1x NuPAGE LDS sample buffer and 1x NuPAGE Sample Reducing Agent), were denatured at 95°C for 10min, and were loaded per gel lane. Protein samples were electrophoresed on NuPAGE Novex 4-12% Bis-Tris Midi protein gels in 1x NuPAGE MOPS SDS running buffer at 200V for 1h at RT. Gels were transferred to nitrocellulose membranes with Tran-Blot Turbo Transfer System (Bio-Rad). Membranes were blocked with Odyssey blocking buffer (Li-Cor 927-40000) at RT for at least 1h, incubated with primary

antibodies overnight at 4°C followed by 4x washes with TBST at RT, and then incubated with secondary antibodies at RT for 1h, followed by 4x washes with TBST at RT. Li-Cor odyssey system was used for western blot detection and quantification. To quantify the calpain activity (Figure 5D), the signal intensity of cleaved α-fodrin band was divided by the sum of band intensities of full-length and cleaved α-fodrin bands (total α-fodrin) per each lane.

Crude Mitochondrial Isolation and Proteinase K treatment

Cultured Neuro-2a or neurons (typically 2-20 million cells) were first rinsed with ice-cold 1x PBS twice and then scraped off in ice-cold 1x PBS. Cells were then spun down at 200rcf at 4°C for 3min and the resulting cell pellets were homogenized in 5ml of ice-cold mitochondrial isolation buffer (220mM mannitol, 70mM sucrose, and 20mM HEPES at pH7.6) by a Dounce homogenizer for 30 strokes per pellet. The homogenates were spun down at 800rcf at 4°C for 10min. The supernatant was transferred to a new tube and further spun down at 10000rcf for 20min at 4°C. The supernatant was collected as the cytoplasmic fraction. The pellet was again dissociated in 1ml of ice-cold mitochondrial isolation buffer and spun down at 10000rcf at 4°C for 20min. The pellet was dissociated in 100μl of ice-cold mitochondrial isolation buffer and collected as the crude mitochondrial fraction. Some of the mitochondrial fraction samples were treated with various concentrations of proteinase K (PK) on ice for 30min. The PK treatment was stopped by adding NuPAGE LDS sample buffer and boiling the samples at 95°C for 10min. Western blot was performed as described in the paragraph above.

Generation of lentivirus encoding WT and E642A SARM1

cDNAs encoding human full-length wildtype (GenBank: Q6SZW1) or E642A (NAD^+-hydrolase dead) SARM1 was cloned into pLVX-EF1α-IRES-puro vector (Clonetech), using EcoRI and BamHI sites. Lentiviruses were produced by SignaGen Laboratories (Lentivirus Production Full Service Pilot Scale: SL100201)

TMRE measurement

Medium of wildtype or SARM1 KO neurons were replaced with pre-warmed Live Cell Imaging Solution (Thermo Fisher Scientific A14291DJ) that contains 200nM TMRE and various concentrations of rotenone, a combination of antimycin/oligomycin, or vehicle. Neurons were then immediately imaged using the Opera Phenix High Content Screening System (PerkinElmer) and images were quantified using the Harmony software (PerkinElmer). To acquire TMRE signal, we used built-in acquisition protocols for Alexa568 (excitation/emission at 561nm/ 570-630nm) and water immersion 63x (NA=1.15) under the confocal mode, every 10min for 3 h at 37°C. TMRE intensity was quantified first by applying the built-in spot analysis to define TMRE-positive puncta. Secondly, corrected spot intensity of TMRE signal was integrated per each spot and then summarized per well. The summarized TMRE intensity was normalized to the mean intensity of the vehicle-treated wildtype well at each time point per biological replicate.

NAD(H) quantification

Equal numbers of wildtype or SARM1 KO neurons plated on 96-well plates were treated with various concentrations of rotenone, a combination of antimycin/oligomycin (Figure 2F), CZ-48, or Vacor (Figure 3F) for 16 hours. Cellular NAD(H) levels were measured using NAD/NADH-Glo assay (Promega). Briefly, neuron plates were cooled down to RT for 30min and the medium volumes were normalized to 50µl per well. The NAD/NADH-Glo detection reagent was prepared while neuron plates were at RT and applied to neuron plates (50µl/well). Plates were incubated at RT for 1h with gentle horizontal shake at 300rpm. Luminescence of each well was measured using EnVision Multimode Plate Reader (PerkinElmer).

Mouse primary dorsal root ganglia (DRG) neuron preparation and NGF-deprivation

Dorsal root ganglia (DRG) were dissected from E12-E14 embryos of CD-1 (Charles River Laboratories) in ice-cold L15 medium. Dissected DRG were trypsinized by resuspending them in Trypsin-EDTA solution with shaking at 300rpm at 37°C for 15min.

After trypsinization, DRG were spun down at 1500rcf at room temperature (RT) for 2min, rinsed once with L15 with 10% HI-FBS, dissociated in L15 with 10% HI-FBS, and triturated by slow pipetting (~20 strokes). Triturated DRG neurons were spun down at 2000rcf at RT for 2min and resuspended in 1ml of the complete DRG medium. The complete DRG medium consists of Neurobasal medium (500ml) supplemented with B27 supplement (10ml), 1M Glucose (20ml), Glutamax (5ml), Penicillin-Streptomycin (10ml, the final concentration: 200U/ml), Nerve growth factor (NGF, the final concentration at 25ng/ml), and 5-floro-2-deoxyuridine (the final concentration at 1μM). The number of viable cells were counted using Cellometer Auto 2000 Cell Viability Counter (Nexcelom). DRG neurons were spun down again at 2000rcf for 2min at RT. Pellet of DRG neurons were resuspended in the appropriate volume of the complete DRG medium so that the concentration of viable cells is 100000/μl. 1.5μl of dissociated DRG neurons were spotted in the middle of wells on 96w plates that are PDL- and laminin-coated. Plates were kept in the tissue-culture incubator (37°C with 5% CO_2 and 95% humidity) for 10 min, and then the complete DRG medium was slowly added to each well (50μl/well). At 1 DIV, DRG neurons were infected with mCherry-encoding lentivirus (SignaGen Laboratories, SL100276) at 20 MOI. At 4-6 DIV, the complete DRG medium was replaced to the NGF-deprivation medium including additional pharmacological treatments. The NGF-deprivation medium consists of Neurobasal medium (500ml) supplemented with B27 supplement (10ml), Glucose (20ml), Glutamax (5ml), Penicillin-Streptomycin (10ml, the final concentration: 200U/ml), 5-floro-2-deoxyuridine (the final concentration at 1μM), anti-NGF antibody (1:100), and CellEvent Caspase-3/7 Green Detection reagent (1:2000).

5h after starting NGF-deprivation, imaging was initiated using the Opera Phenix High Content Screening System (PerkinElmer). To acquire fluorescent images, we used built-in acquisition protocols for Alexa488 (excitation/emission at 488nm/ 500-550nm) and Alexa568 (561nm/ 570-630nm) and 10x objective (NA=0.3) under the confocal mode. Images were taken every 1h with the chamber temperature set at 37°C with 5% CO_2. Images were quantified using the Harmony software (PerkinElmer). To quantify caspase-positive nuclei, we first defined nuclei based on the mCherry fluorescence by applying built-in nuclear detection method to images on the Alexa568 channel.

Secondly, the mean intensity of CellEvent Caspase-3/7 Green Detection reagent (CellEvent) was quantified in each nucleus. Lastly, the proportion of Casapse3/7-positive nuclei was quantified per each well by defining the background level of CellEvent intensity in the control condition (e.g. neurons that were not deprived of NGF) in each experiment and counting the numbers of nuclei that have higher CellEvent intensity than background.

Synthesis of CZ-48, PC6, and SARM1 inhibitor

CZ-48 (Chen et al., 2011), PC6 (Li et al., 2021), and SARM1 inhibitor 3-iodo-1H-pyrrolo[2,3-c]pyridine (Hughes et al., 2019) were synthesized by following the methods described previously.

Mouse Handling

All mouse procedures adhered to regulations and protocols approved by Denali Therapeutics Institutional Animal Care and Use Committee. Mice were housed under a 12-hour light/dark cycle and had access to water and standard rodent diet *ad libitum*.

Experimental Design and Statistical Analysis

Each experiment consists of all the conditions that were directly compared, including genotype, variable doses of toxin treatment, and the presence of pharmacological treatment. Each condition consists of 1-3 technical replicates, such as wells (western blot and immunocytochemistry) and mitochondria (Figure 1C-E). Bulk of data were acquired and analyzed by automated systems in an unbiased manner. Super-resolution microscopy (Figure 1C-E) and western blot (Figures 1B and 5C) experiments were performed and analyzed in a non-blinded manner. Acquired data were averaged and/or normalized to the control condition (e.g. DMSO-treated wildtype neurons) in each experiment. We then repeated experiments using biologically distinct samples, which indicate neurons prepared from different mice on a different day (typically one to several weeks apart), or cells independently plated and transfected (Figure 1). Averaged and/or normalized values from each biologically independent replicate was treated as independent unit (n), plotted, and reported in each Figure legend.

Statistical tests were performed by ANOVA using stats::aov function in R (Version 4.1.2) and independent variables were reported in Figure legend. An interaction effect between two independent variables were also assessed when running two-way ANOVA. In most Figures, P values of the main effect were indicated in Figure panels with two significant figures up to three decimal places. In Figures 5F, 5G, and 6C, P values are for the difference between each experimental group against the control group, determined by Dunnett's post-hoc test using contrast function from the emmeans R package (Lenth, 2022).

Table 2: Key Reagents

Acronym	Reagents	Source	Identifier
1x PBS	PBS, pH7.4	Thermo Fisher Scientific	10010023
5-Fluoro-2'deoxyuridine	5-Fluoro-2'deoxyuridine	Sigma-Aldrich	856657
Antimycin	Antimycin A from Streptomyces sp.	Sigma-Aldrich	A8674
B27	B27 Supplement (50x), serum free	Thermo Fisher Scientific	17504044
Biocoat 96-well plates	BioCoat Poly-D-Lysine 96-well Black/Clear plates	Corning	354640
Biocoat 384-well plates	BioCoat Poly-D-Lysine 384-well Black/Clear flat bottom plates	Corning	354663
BSA	Bovine Serum Albumin	Sigma-Aldrich	A2153
Calpain Inhibitor III	Calpain Inhibitor III	Sigma-Aldrich	208722
CellEvent Caspase-3/7 Green Detection reagent	CellEvent Caspase-3/7 Green Detection reagent	Thermo Fisher Scientific	C10423
Cell Mask	CellMask Depp Red Plasma Membrane Stain	Thermo Fisher Scientific	C10046
CZ-48	CZ-48	Synthesized. See Methods	CAS: 1374663-29-2
DAPI	DAPI solution (1mg/ml)	Thermo Fisher Scientific	62248
DNAseI	Deoxyribonuclease I from bovine pancreas	Sigma-Aldrich	D5025-150KU
EGTA	EGTA 1M, pH8.0, Sterile	BioWorld	40120128-1
FK866	FK 866 hydrochloride	Tocris	4808/10
Glucose	1M Glucose	Boston BioProducts	BM-675
Glutamax	GlutaMAX™ Supplement	Thermo Fisher Scientific	35050061
GNE-3511	GNE-3511	MedKoo Biosciences	522419
HI-FBS	Heat-inactivated fatal bovine serum	VWR	97068-085
Hibernate E	Hibernate E - Calcium -Magnesium	BrainBits	HECAMG500
L15	Leibovitz's L-15 medium	Thermo Fisher Scientific	11415064
Laminin	Natural Mouse Laminin	Thermo Fisher Scientific	23017015
Live Cell Imaging Solution	Live Cell Imaging Solution	Thermo Fisher Scientific	A14291DJ
NAD/NADH-Glo assay	NAD/NADH-Glo assay	Promega	G9072
NbActiv4	NbActiv4 (for primary neuron cultures)	BrainBits	Nb4-500
NGF	Nerve Growth Factor, NGF 2.5S Murine	Promega	G514A
Anti-NGF antibody	Anti-Nerve Growth Factor-β antibody	Millipore Sigma	AB1528 (RRID: AB_90740)
mCherry lentivirus	LV-CMV-mCherry-Puro	SignaGen Laboratories	SL100276
Neurobasal medium	Neurobasal Medium	Thermo Fisher Scientific	21103049
NuPAGE LDS sample buffer	NuPAGE LDS Sample Buffer (4x)	Thermo Fisher Scientific	NP0007
NuPAGE MOPS SDS running buffer	NuPAGE MOPS SDS running buffer	Thermo Fisher Scientific	MP000102
NuPAGE Novex 4-12% Bis-Tris Midi protein gels	NuPAGE Novex 4-12% Bis-Tris Midi protein gels	Thermo Fisher Scientific	WG1403
NuPAGE Sample Reducing Agent	NuPAGE Sample Reducing Agent (10x)	Thermo Fisher Scientific	NP0009

Oligomycin	Oligomycin from Streptomyces diastatochoromogenes	Sigma-Aldrich	O4876
Papain	PDS Kit, Papain vial	Worthington	LK003178
Paraformaldehyde (PFA)	32% PFA	Electron Microscopy Sciences	15714-S
PC6	PC6	Synthesized. See Methods	(Li et al., 2021)
Penicillin-Streptomycin	Penicillin-Streptomycin (10000U/ml)	Thermo Fisher Scientific	15140122
PK	Proteinase K	Promega	MC5008
QVD	Q-VD-OPh hydrate	Sigma-Aldrich	SML0063-1MG
Rotenone	Rotenone	Sigma-Aldrich	R8875
Sucrose	Sucrose	Sigma-Aldrich	S0389
TBST	Tris-buffered saline with 0.5% Tween20	Teknova	T9501
TMRE	Tetramethylrhodamine, Ethyl Ester, Perchlorate	Abcam	Ab113852
Trans-Blot Turbo Transfer System	Trans-Blot Turbo Transfer System, 0.2µm Nitrocellulose	Bio-Rad	1704270
Triton X100	Triton X-100	Thermo Fisher Scientific	BP151-500
Trypsin-EDTA	Trypsin-EDTA (0.05%), phenol red	Thermo Fisher Scientific	25300054
Vacor	Pyrinuron	Chem Service	N-13738

Acknowledgements

We thank Thomas Sandmann for statistical analysis support and manuscript feedback. We also thank members of Denali Therapeutics for helpful discussions and comments on the manuscript.

Competing Interests

All authors are paid employees and shareholders of Denali Therapeutics.

References

Araki T, Sasaki Y, Milbrandt J. 2004. Increased Nuclear NAD Biosynthesis and SIRT1 Activation Prevent Axonal Degeneration. *Science* **305**:1010–1013. doi:10.1126/science.1098014

Avery MA, Rooney TM, Pandya JD, Wishart TM, Gillingwater TH, Geddes JW, Sullivan PG, Freeman MR. 2012. Wld S prevents axon degeneration through increased mitochondrial flux and enhanced mitochondrial Ca^{2+} buffering. *Curr Biol* **22**:596–600. doi:10.1016/j.cub.2012.02.043

Babetto E, Beirowski B, Janeckova L, Brown R, Gilley J, Thomson D, Ribchester RR, Coleman MP. 2010. Targeting NMNAT1 to axons and synapses transforms its neuroprotective potency in vivo. *J Neurosci* **30**:13291–13304. doi:10.1523/JNEUROSCI.1189-10.2010

Bratkowski M, Xie T, Thayer DA, Lad S, Mathur P, Yang YS, Danko G, Burdett TC, Danao J, Cantor A, Kozak JA, Brown SP, Bai X, Sambashivan S. 2020. Structural and mechanistic regulation of the pro-degenerative NAD hydrolase SARM1. *Cell Rep* **32**. doi:10.1016/j.celrep.2020.107999

Buonvicino D, Mazzola F, Zamporlini F, Resta F, Ranieri G, Camaioni E, Muzzi M, Zecchi R, Pieraccini G, Dölle C, Calamante M, Bartolucci G, Ziegler M, Stecca B, Raffaelli N, Chiarugi A. 2018. Identification of the nicotinamide salvage pathway as a new toxification route for antimetabolites. *Cell Chem Biol* **25**:471-482.e7. doi:10.1016/j.chembiol.2018.01.012

Chen Z, Kwong AKY, Yang Z, Zhang LL, Lee HC, Zhang LL. 2011. Studies on the synthesis of nicotinamide nucleoside and nucleotide analogues and their inhibitions towards CD38 NADase. *Heterocycles* **83**:2837–2850. doi:10.3987/COM-11-12361

Coleman MP, Höke A. 2020. Programmed axon degeneration: from mouse to mechanism to medicine. *Nat Rev Neurosci* **21**:183–196. doi:10.1038/s41583-020-0269-3

Conforti L, Wilbrey A, Morreale G, Janeckova L, Beirowski B, Adalbert R, Mazzola F, Stefano M Di, Hartley R, Babetto E, Smith T, Gilley J, Billington RA, Genazzani AA, Ribchester RR, Magni G, Coleman M. 2009. Wld S protein requires Nmnat activity and a short N-terminal sequence to protect axons in mice. *J Cell Biol* **184**:491–500.

doi:10.1083/jcb.200807175

Cryns VL, Bergeron L, Zhu H, Li H, Yuan J. 1996. Specific cleavage of α-fodrin during fas- and tumor necrosis factor- induced apoptosis is mediated by an interleukin-1β-converting enzyme/Ced-3 protease distinct from the poly(ADP-ribose) polymerase protease. *J Biol Chem* **271**:31277–31282. doi:10.1074/jbc.271.49.31277

Di Stefano M, Nascimento-Ferreira I, Orsomando G, Mori V, Gilley J, Brown R, Janeckova L, Vargas ME, Worrell LA, Loreto A, Tickle J, Patrick J, Webster JRM, Marangoni M, Carpi FM, Pucciarelli S, Rossi F, Meng W, Sagasti A, Ribchester RR, Magni G, Coleman MP, Conforti L. 2015. A rise in NAD precursor nicotinamide mononucleotide (NMN) after injury promotes axon degeneration. *Cell Death Differ* **22**:731–742. doi:10.1038/cdd.2014.164

Dudek J, Rehling P, van der Laan M. 2013. Mitochondrial protein import: Common principles and physiological networks. *Biochim Biophys Acta - Mol Cell Res* **1833**:274–285. doi:10.1016/j.bbamcr.2012.05.028

Essuman K, Summers DW, Sasaki Y, Mao X, Diantonio A, Milbrandt J. 2017. The SARM1 Toll / Interleukin-1 receptor domain possesses intrinsic NAD^+ cleavage activity that promotes pathological axonal degeneration. *Neuron* **93**:1334-1343.e5. doi:10.1016/j.neuron.2017.02.022

Essuman K, Summers DW, Sasaki Y, Mao X, Yim AKY, DiAntonio A, Milbrandt J. 2018. TIR domain proteins are an ancient family of NAD+-consuming enzymes. *Curr Biol* 1–10. doi:10.1016/j.cub.2017.12.024

Figley MD, Gu W, Nanson JD, Shi Y, Sasaki Y, Cunnea K, Malde AK, Jia X, Luo Z, Saikot FK, Mosaiab T, Masic V, Holt S, Hartley-Tassell L, McGuinness HY, Manik MK, Bosanac T, Landsberg MJ, Kerry PS, Mobli M, Hughes RO, Milbrandt J, Kobe B, DiAntonio A, Ve T. 2021. SARM1 is a metabolic sensor activated by an increased NMN/NAD^+ ratio to trigger axon degeneration. *Neuron* **109**:1118-1136.e11. doi:10.1016/j.neuron.2021.02.009

Geisler S, Doan RA, Cheng GC, Cetinkaya-Fisgin A, Huang SX, Höke A, Milbrandt J, DiAntonio A. 2019. Vincristine and bortezomib use distinct upstream mechanisms to activate a common SARM1-dependent axon degeneration program **4**:e129920. doi:10.1172/jci.insight.129920

Gerdts J, Brace EJ, Sasaki Y, DiAntonio A, Milbrandt J. 2015. SARM1 activation triggers axon degeneration locally via NAD^+ destruction. *Science* **348**:453–457. doi:10.1126/science.1258366

Gerdts J, Summers DW, Milbrandt J, DiAntonio A. 2016. Axon self-destruction: new links among SARM1, MAPKs, and NAD+ metabolism. *Neuron* **89**:449–460. doi:10.1016/j.neuron.2015.12.023

Gerdts J, Summers DW, Sasaki Y, DiAntonio A, Milbrandt J. 2013. Sarm1-mediated axon degeneration requires both SAM and TIR interactions. *J Neurosci* **33**:13569–80. doi:10.1523/JNEUROSCI.1197-13.2013

Ghosh AS, Wang B, Pozniak CD, Chen M, Watts RJ, Lewcock JW. 2011. DLK induces developmental neuronal degeneration via selective regulation of proapoptotic JNK activity. *J Cell Biol* **194**:751–764. doi:10.1083/jcb.201103153

Gilley J, Coleman MP. 2010. Endogenous Nmnat2 Is an Essential Survival Factor for Maintenance of Healthy Axons. *PLoS Biol* **8**:e1000300. doi:10.1371/journal.pbio.1000300

Horsefield S, Burdett H, Zhang X, Manik MK, Shi Y, Chen J, Qi T, Gilley J, Lai JS, Rank MX, Casey LW, Gu W, Ericsson DJ, Foley G, Hughes RO, Bosanac T, Von Itzstein M, Rathjen JP, Nanson JD, Boden M, Dry IB, Williams SJ, Staskawicz BJ, Coleman MP, Ve T, Dodds PN, Kobe B. 2019. NAD^+ cleavage activity by animal and plant TIR domains in cell death pathways. *Science* **365**:793–799. doi:10.1126/science.aax1911

Hughes RO, Devraj R, Bosanac T, Jarjes-pike RA, Brearley AS, Bentley J. 2019. Inhibitors of Sarm1. WO2019236884A1.

Jiang Y, Liu T, Lee CH, Chang Q, Yang J, Zhang Z. 2020. The NAD^+-mediated self-inhibition mechanism of pro-neurodegenerative SARM1. *Nature* **588**:658–663. doi:10.1038/s41586-020-2862-z

Kim Y, Zhou P, Qian L, Chuang J-Z, Lee J, Li C, Iadecola C, Nathan C, Ding A. 2007. MyD88-5 links mitochondria, microtubules, and JNK3 in neurons and regulates neuronal survival. *J Exp Med* **204**:2063–2074. doi:10.1084/jem.20070868

Krauss R, Bosanac T, Devraj R, Engber T, Hughes RO. 2020. Axons matter: the promise of treating neurodegenerative disorders by targeting SARM1-mediated

axonal degeneration. *Trends Pharmacol Sci* **41**:281–293. doi:10.1016/j.tips.2020.01.006

Lenth R V. 2022. emmeans: Estimated marginal means, aka least-squares means.

Li WH, Huang K, Cai Y, Wang QW, Zhu WJ, Hou YN, Wang S, Cao S, Zhao ZY, Xie XJ, Du Y, Lee CS, Lee HC, Zhang H, Zhao YJ. 2021. Permeant fluorescent probes visualize the activation of SARM1 and uncover an anti-neurodegenerative drug candidate. *eLife* **10**:1–21. doi:10.7554/eLife.67381

Loreto A, Angeletti C, Gu W, Osborne A, Nieuwenhuis B, Gilley J, Merlini E, Arthur-Farraj P, Amici A, Luo Z, Hartley-Tassell L, Ve T, Desrochers LM, Wang Q, Kobe B, Orsomando G, Coleman MP. 2021. Neurotoxin-mediated potent activation of the axon degeneration regulator SARM1. *eLife* **10**:1–24. doi:10.7554/elife.72823

Loreto A, Di Stefano M, Gering M, Conforti L. 2015. Wallerian degeneration Is executed by an NMN-SARM1-dependent late Ca2+ Influx but only modestly influenced by mitochondria. *Cell Rep* **13**:2539–2552. doi:10.1016/j.celrep.2015.11.032

Loreto A, Hill CS, Hewitt VL, Orsomando G, Angeletti C, Gilley J, Lucci C, Sanchez-Martinez A, Whitworth AJ, Conforti L, Dajas-Bailador F, Coleman MP. 2020. Mitochondrial impairment activates the Wallerian pathway through depletion of NMNAT2 leading to SARM1-dependent axon degeneration. *Neurobiol Dis* **134**:104678. doi:10.1016/j.nbd.2019.104678

Loring HS, Icso JD, Nemmara V, Thompson PR. 2020. Initial kinetic characterization of sterile alpha and toll/interleukin receptor motif-containing protein 1. *Biochemistry* **59**:933–942. doi:10.1021/acs.biochem.9b01078

Lunn ER, Perry VH, Brown MC, Rosen H, Gordon S. 1989. Absence of Wallerian degeneration does not hinder regeneration in peripheral nerve. *Eur J Neurosci* **1**:27–33. doi:10.1111/j.1460-9568.1989.tb00771.x

Mack TG, Reiner M, Beirowski B, Mi W, Emanuelli M, Wagner D, Thomson D, Gillingwater T, Court F, Conforti L, Fernando FS, Tarlton A, Andressen C, Addicks K, Magni G, Ribchester RR, Perry VH, Coleman MP. 2001. Wallerian degeneration of injured axons and synapses is delayed by a Ube4b/Nmnat chimeric gene. *Nat Neurosci* **4**:1199–1206. doi:10.1038/nn770

Metwally E, Zhao G, Zhang YQ. 2021. The calcium-dependent protease calpain in

neuronal remodeling and neurodegeneration. *Trends Neurosci* **44**:741–752. doi:10.1016/j.tins.2021.07.003

Mishra B, Carson R, Hume RI, Collins CA. 2013. Sodium and potassium currents influence wallerian degeneration of injured Drosophila axons. *J Neurosci* **33**:18728–18739. doi:10.1523/JNEUROSCI.1007-13.2013

Osterloh JM, Yang J, Rooney TM, Fox AN, Adalbert R, Powell EH, Sheehan AE, Avery M a, Hackett R, Logan M a, MacDonald JM, Ziegenfuss JS, Milde S, Hou Y-J, Nathan C, Ding A, Brown RH, Conforti L, Coleman M, Tessier-Lavigne M, Züchner S, Freeman MR. 2012. dSarm/Sarm1 is required for activation of an injury-induced axon death pathway. *Science* **337**:481–4. doi:10.1126/science.1223899

Panneerselvam P, Singh LP, Ho B, Chen J, Ling J. 2012. Targeting of pro-apoptotic TLR adaptor SARM to mitochondria: definition of the critical region and residues in the signal sequence. *Biochem J* **442**:263–271. doi:10.1042/BJ20111653

Rueden CT, Schindelin J, Hiner MC, DeZonia BE, Walter AE, Arena ET, Eliceiri KW. 2017. ImageJ2: ImageJ for the next generation of scientific image data. *BMC Bioinformatics* **18**:1–26. doi:10.1186/s12859-017-1934-z

Sasaki Y, Engber TM, Hughes RO, Figley MD, Wu T, Bosanac T, Devraj R, Milbrandt J, Krauss R, DiAntonio A. 2020. cADPR is a gene dosage-sensitive biomarker of SARM1 activity in healthy, compromised, and degenerating axons. *Exp Neurol* **329**:113252. doi:10.1016/j.expneurol.2020.113252

Sasaki Y, Vohra BPS, Baloh RH, Milbrandt J. 2009. Transgenic mice expressing the Nmnat1 protein manifest robust delay in axonal degeneration in vivo. *J Neurosci* **29**:6526–6534. doi:10.1523/JNEUROSCI.1429-09.2009

Seager R, Lee L, Henley JM, Wilkinson KA. 2020. Mechanisms and roles of mitochondrial localisation and dynamics in neuronal function. *Neuronal Signal* **4**:1–28. doi:10.1042/ns20200008

Shen C, Vohra M, Zhang P, Mao X, Figley MD, Zhu J, Sasaki Y, Wu H, DiAntonio A, Milbrandt J. 2021. Multiple domain interfaces mediate SARM1 autoinhibition. *Proc Natl Acad Sci U S A* **118**:1–9. doi:10.1073/pnas.2023151118

Simon DJ, Weimer RM, Mclaughlin T, Kallop D, Stanger K, Yang J, O'Leary DDM, Hannoush RN, Tessier-Lavigne M. 2012. A caspase cascade regulating

developmental axon degeneration. *J Neurosci* **32**:17540–17553. doi:10.1523/JNEUROSCI.3012-12.2012

Sporny M, Guez-Haddad J, Khazma T, Yaron A, Dessau M, Shkolnisky Y, Mim C, Isupov MN, Zalk R, Hons M, Opatowsky Y. 2020. Structural basis for SARM1 inhibition and activation under energetic stress. *eLife* **9**:1–25. doi:10.7554/eLife.62021

Summers DW, DiAntonio A, Milbrandt J. 2014. Mitochondrial dysfunction induces Sarm1-dependent cell death in sensory neurons. *J Neurosci* **34**:9338–9350. doi:10.1523/JNEUROSCI.0877-14.2014

Summers DW, Frey E, Walker LJ, Milbrandt J, DiAntonio A. 2020. DLK activation synergizes with mitochondrial dysfunction to downregulate axon survival factors and promote SARM1-dependent axon degeneration. *Mol Neurobiol* **57**:1146–1158. doi:10.1007/s12035-019-01796-2

Sur M, Dey P, Sarkar A, Bar S, Banerjee D, Bhat S, Mukherjee P. 2018. Sarm1 induction and accompanying inflammatory response mediates age-dependent susceptibility to rotenone-induced neurotoxicity. *Cell Death Discov* **4**. doi:10.1038/s41420-018-0119-5

Tian W, Czopka T, López-Schier H. 2020. Systemic loss of Sarm1 protects Schwann cells from chemotoxicity by delaying axon degeneration. *Commun Biol* **3**:1–14. doi:10.1038/s42003-020-0776-9

Vargas ME, Yamagishi Y, Tessier-Lavigne M, Sagasti A. 2015. Live imaging of calcium dynamics during axon degeneration reveals two functionally distinct phases of calcium influx. *J Neurosci* **35**:15026–15038. doi:10.1523/JNEUROSCI.2484-15.2015

Verdin E. 2015. NAD^+ in aging, metabolism, and neurodegeneration. *Science* **350**:1208–1213. doi:10.1126/science.aac4854

Watkins TA, Wang B, Huntwork-Rodriguez S, Yang J, Jiang Z, Eastham-Anderson J, Modrusan Z, Kaminker JS, Tessier-Lavigne M, Lewcock JW. 2013. DLK initiates a transcriptional program that couples apoptotic and regenerative responses to axonal injury. *Proc Natl Acad Sci U S A* **110**:4039–4044. doi:10.1073/pnas.1211074110

Yang J, Weimer RM, Kallop D, Olsen O, Wu Z, Renier N, Uryu K, Tessier-Lavigne M. 2013. Regulation of axon degeneration after injury and in development by the endogenous calpain inhibitor calpastatin. *Neuron* **80**:1175–1189. doi:10.1016/j.neuron.2013.08.034

Yang J, Wu Z, Renier N, Simon DJ, Uryu K, Park DS, Greer PA, Tournier C, Davis RJ, Tessier-Lavigne M. 2015. Pathological axonal death through a Mapk cascade that triggers a local energy deficit. *Cell* **160**:161–176. doi:10.1016/j.cell.2014.11.053

Zhao ZY, Xie XJ, Li WH, Liu J, Chen Z, Zhang B, Li T, Li SL, Lu JG, Zhang Liangren, Zhang Li he, Xu Z, Lee HC, Zhao YJ. 2019. A cell-permeant mimetic of NMN activates SARM1 to produce cyclic ADP-ribose and induce non-apoptotic cell death. *iScience* **15**:452–466. doi:10.1016/j.isci.2019.05.001